5.9 **Photon-coupled traps:** In the text we mention the possibility of coupling different traps with the use of photons. We explore this idea further in this exercise. Consider two traps, each with an ion labelled the **communication ion**. These two ions are irradiated, emitting a photon whose frequency depends on the ion's state. If the ion is in the ground state $|0\rangle$, the photon is blue ($\hat{a}^\dagger_{\text{blue}}|0\rangle_k =: |\nu_{\text{blue}}\rangle$). If the ion is in the ground state $|1\rangle$ the photon is red ($\hat{a}^\dagger_{\text{red}}|0\rangle_k =: |\nu_{\text{red}}\rangle$). The photons arrive at a 50/50 beam splitter. We then measure one photon at each detector. The measurements are done in the Bell basis. What Bell state needs to be measured for the two ions to be entangled? What is the final state of the communication ions?

5.10 **Ramsey interferometry with ions:** An early application of trapped-ion quantum computers was metrology, the science of more precise measurements. One notable example of this is Ramsey interferometry. Say you begin with a single ion in the ground state, $|0\rangle$. If left to evolve for some time t, the ion's excited state will accumulate a phase ϕ relative to the ground state. With only the use of single-qubit rotations and projective measurements, create a protocol to determine ϕ.

6 Superconducting Circuits

In the previous chapters we selected our qubits from natural systems: nuclear spins, photons, and ions. By doing so, we worked with qubits that have fixed properties. However, what could we do if we could tune the parameters of these qubits to more convenient values? We will take this idea further by building qubits using a similar approach to classical computing.

As a first guess, we can try to build a qubit from an electrical circuit – for instance, an LC oscillator. By doing so, we could tune the energy levels of our qubit by modifying the capacitance or the inductance. However, this approach would present two challenges. The first is that conventional LC circuits have an internal resistance that would induce decoherence in the quantum setting. The second is that an LC circuit is a harmonic oscillator, which means that the energy difference between energy levels is constant, so it's challenging to isolate two energy levels to use as our qubit. Fortunately, we can solve these challenges by using superconducting materials and making tunable qubits, known as **superconducting qubits**.

This chapter introduces how we can use superconducting qubits for quantum computing. We begin with a brief introduction to superconductivity (Section 6.1) and superconducting circuits (Section 6.2). This section introduces a critical circuit element called the Josephson junction. In Section 6.3 we see how we can use it to build an electrical circuit with an energy spectrum suitable to construct a qubit. There are many types of superconducting qubits. This chapter focuses on the transmon and briefly mentions other superconducting qubit architectures. We will initialize the transmon using brute-force cooling machines called dilution refrigerators (Section 6.5). In Section 6.4 we introduce the field of circuit quantum electrodynamics (QED). With this, we can then explain how the qubits are controlled (Section 6.6) and measured (Section 6.7). Next, we discuss the noise sources in Section 6.8. Like in Chapter 3, we use concrete examples to discuss noise in superconducting qubits, but the methods outlined here are general and can be applied to other types of qubits. We conclude in Section 6.9 with a summary of the chapter and an overview of the strengths and weaknesses of superconducting qubit quantum computing.

6.1 Superconductivity

Superconductors have enabled many technologies. We've seen examples of this in earlier chapters. In NMR we found they can be used to produce powerful magnetic fields. In optics we found they can operate as sensitive detectors. To study superconducting qubits,

we'll need a more detailed introduction to the properties of superconductors and a theory that explains how these properties emerge. We introduce two characteristic macroscopic properties of superconductivity in Section 6.1.1. In Section 6.1.2 we outline the Bardeen–Cooper–Schrieffer (BCS) theory of superconductivity that describes how superconductivity emerges from microscopic effects. We conclude this section by demonstrating an important property of superconducting systems: Magnetic flux can be quantized under the right conditions (Section 6.1.3).

6.1.1 Properties of Superconductors

Quantum mechanics is usually thought of as the physics of very small things; superconductivity challenges this notion. Superconductivity is characterized by two distinct macroscopic properties: perfect conductivity and perfect **diamagnetism**. (A diamagnetic material partially expels external magnetic fields.)

Most metals are superconductors at sufficiently low temperatures. There are different types of superconductors. Here, we will consider conventional **low-temperature superconductors** described by BCS theory. Metallic elements, such as aluminum or niobium, or alloys of these, such as niobium–titanium, are the typical low-temperature superconductors. The more exotic **high-temperature superconductors** are made from ceramic materials doped into a conducting state.

The perfect conductivity of superconductors was discovered by Heike Kamerlingh Onnes in 1911, earning him the Nobel Prize in 1913 for his discovery. This discovery was enabled by Onnes' earlier discovery of a process to liquefy helium and achieve the record low temperatures necessary for discovering superconductors. It had previously been observed that the resistivity of metals decreased smoothly as they were cooled, but what Onnes was surprised to find was that, as the temperature dropped below 4.2 K, the resistance of mercury suddenly dropped to zero (Fig. 6.1). The temperature where this sudden drop occurs is

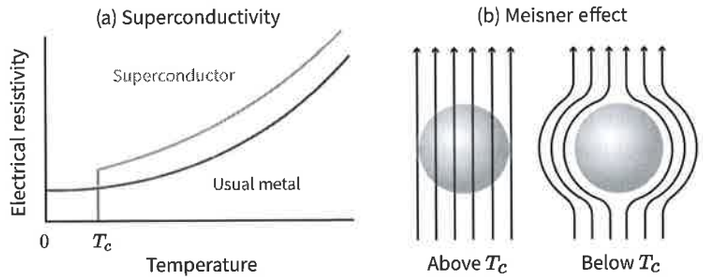

Fig. 6.1 **Superconductivity and the Meissner effect.** (a) Sketch of the electrical resistivity of typical metals plotted against temperature. Superconducting systems are distinguished by their resistivity suddenly dropping to zero at a critical temperature, T_c. (b) Diagram of the Meissner effect. Once a system becomes superconducting, it expels all external magnetic field lines.

known as the **critical temperature**, T_c. It was later understood that this change represented a **phase transition**[1] of the conduction electrons in the metal.

The perfect diamagnetism of superconductors was later discovered by Walther Meissner and Robert Ochsenfeld, in 1933. Meissner and Ochsenfeld found that superconductors expel externally applied magnetic fields when cooled through their critical temperature. This expulsion of magnetic fields is known as the **Meissner effect**. It is what enables the popular science demonstration of superconductors levitating magnets. It's important to emphasize that perfect diamagnetism is distinct from perfect conductivity, although the difference can be subtle. Classical electromagnetism allows a magnetic field to become trapped in a perfect conductor. That is, according to **Lenz's law** (which says that a changing magnetic field induces a voltage which will drive a current in a conductor that opposes the change in the magnetic field), if a cooled metal became a perfect conductor, it would trap an externally applied magnetic field inside of it. However, Meissner and Ochsenfeld found this was not true in superconductors. The magnetic field is expelled from them. This implies that the Meissner effect is not a consequence of perfect conductivity but is a distinct effect. The microscopic mechanism of the Meissner effect is that the superconductor generates a screening current on its surface that shields the body of the superconductor from the existing external field.

Superconductors are characterized by three critical parameters that describe the external conditions necessary for the metal to be superconducting. The most recognized of these conditions is that the material must be cooled below a particular temperature; this is the critical temperature, which is mostly in the range of 0–20 K for low-temperature superconductors. The second parameter is that the strength of the magnetic field surrounding the superconductor must be below a certain point, known as the **critical field**, H_c.[2] It is typically in the range 10^{-1}–10^{1} T. The final parameter is that the electrical current passing through the metal must be below a **critical current**, I_c. Since I_c depends on the cross-sectional area of the metal, A, we often talk about the critical current density $J_c = I_c/A$, which is an intrinsic property. The critical current density of typical low-temperature superconductors is in the range of 10^2–10^4 A/mm^2. While the values of these three critical parameters depend on the microscopic details of the superconductor, they are all a proxy for the superconductivity's "strength" in the metal. Therefore, these parameters are highly correlated and depend on each other. We define these critical parameters as the maximum value when only one external condition is applied. These values won't be observed if more than one external condition is applied. For example, the maximum observed supercurrent depends on the magnetic field and temperature. This dependence is important in applications such as the high-field magnets used in NMR. A current produces a magnetic field in this application, but the resulting magnetic field will reduce the critical current.

[1] A phase transition is an abrupt change in a system's properties in response to a change in one or more of the system's macroscopic variables, e.g. a solid melting into a liquid due to a temperature change.

[2] Here, H is used instead of B because it relates to the magnetic field in materials.

6.1.2 BCS Theory of Superconductivity

The Bardeen–Cooper–Schrieffer (BCS) theory of superconductivity describes how superconductivity emerges in conventional metals from microscopic effects. This theory was proposed in 1957 by John Bardeen, Leon Cooper, and John Robert Schrieffer, 46 years after the discovery of superconductivity. They were awarded the Nobel Prize for this work in 1972. While we won't explore the details of BCS theory, we will use its main result, that superconductivity emerges due to the formation of pairs of electrons.

Cooper Pairs

Cooper pairs are pairs of electrons that, at low temperatures, experience a weak attractive coupling to one another. In 1956, Leon Cooper proved that the electrons could lower their energy compared to the normal-metal ground state by forming bound pairs, even if the attractive potential is weak. The exact form of the interaction is quite complex mathematically. However, it was understood early on that it was likely that the crystal lattice's phonons were mediating the attractive interaction between electrons. The role of the crystal lattice in superconductivity was confirmed by the discovery of the **isotope effect**, which showed that bulk superconducting properties, such as T_c and H_c, change with the isotopic mass of the ions in the lattice.

Despite the complexity of a rigorous mathematical description, there is an intuitive picture of the microscopic origin of the attractive electron potential that produces Cooper pairs. Inside a metal, the negative charge of the conduction electrons is balanced by the positive charge of the ions that make up the crystal lattice. This balance makes the total system charge neutral on average. However, on short timescales, an electron passing through the lattice of positive ions will pull the ions toward it (Fig. 6.2). This will result in the electron leaving a slightly positive charge density trail behind it. This region of positive charge can attract a second electron, thus giving rise to an attractive electron–electron interaction. The two electrons correlated by the lattice deformation can have a separation of 100 nm or more, much larger than the distance between the ions in the lattice, which is ~0.1 nm. In fully quantum language, we would describe the interaction as arising from the exchange

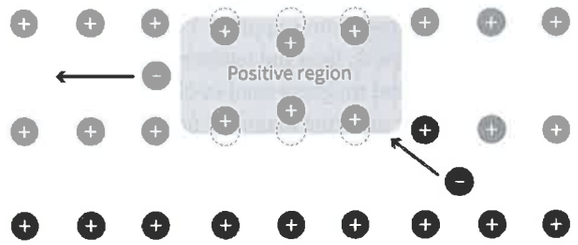

Fig. 6.2 **Depiction of the attractive interaction that forms Cooper pairs.** A moving electron attracts the positively charged ions in the lattice. The lattice is slightly distorted, creating a positively charged region in the wake of the moving electron. Another electron is attracted to that region, creating an effective coupling between the two electrons.

of phonons between the two electrons, in analogy to how electrons interact by exchanging photons in quantum electrodynamics.

BCS Ground State and Condensate Wavefunction

More than 45 years elapsed between the experimental discovery of superconductivity and its explanation by the BCS theory. Part of the difficulty was the complexity of the phonon-mediated interaction between the electrons. BCS cleverly avoided these details. They "guessed" the form of the ground-state wavefunction of the superconducting state with unknown coefficients characterizing the probability amplitudes of particular momentum states being occupied or unoccupied by Cooper pairs. They then used variational techniques to minimize the energy of this ansatz wavefunction in terms of the probability amplitudes. With an explicit form for the probability amplitudes, they now had the complete form of the BCS ground-state wavefunction. The variational technique used by BCS has become an important tool in theoretical physics. For instance, it was used by Robert Laughlin to derive the ground-state wavefunction of the fractional quantum Hall effect, earning him the Nobel Prize in 1998.

The BCS ground-state wavefunction describes a collection of globally phase-coherent electrons. That is, the quantum phase of each Cooper pair has a well-defined relation to every other. In this way, the Cooper pairs form a macroscopic quantum state often referred to as the **BCS condensate**. This is very different from the normal (not superconducting) state of electrons in a metal, where the constant scattering of electrons by the crystal lattice and other electrons scrambles the electrons' phases, leaving them largely incoherent. The emergence of phase coherence in the BCS condensate, therefore, hints at the suppression of electron scattering. This is formalized in the BCS theory by the emergence of an energy gap, Δ_{BCS}, between the BCS ground state and the first excited state of the electronic system. This energy gap, related to the binding energy of the Cooper pairs, means that Cooper pairs are immune to low-energy scattering events that scramble the phases of the normal-state electrons and cause electrical resistance in normal metals. This suppression of scattering gives rise to the perfect conductivity of the superconducting state. Furthermore, the global coherence of the phases of the Cooper pairs in the condensate, along with the fundamental coupling of the electron's phase to the magnetic vector potential, gives rise to the unusual magnetic properties of superconductors.

It's possible to understand many of the macroscopic properties of superconductors by postulating that a single wavefunction describes the condensate of Cooper pairs. We will follow this phenomenological approach here, inspired by the Feynman Lectures on Physics. Still, we note that the concept of the macroscopic condensate wavefunction can be made rigorous by a theory invented by two Russian physicists, Vitaly Ginzburg and Lev Landau. The Ginzburg–Landau theory derived the properties of the superconducting condensate by treating the onset of superconductivity as a phase transition of the electrons, using the more general Landau theory of phase transitions. The Ginzburg–Landau theory was published in the former Soviet Union in 1950 but didn't receive much attention in the West until a few decades later.

In this treatment, we start by writing the macroscopic wavefunction for the superconducting condensate, $\psi(\vec{r})$, where $\vec{r}$ is the position within the superconductor. We define $\rho(\vec{r}) = \psi(\vec{r})^*\psi(\vec{r})$, which is the modulus square of the wavefunction, as the density of Cooper pairs. Finally, we can write the full wavefunction as

$$\psi(\vec{r}) = \sqrt{\rho(\vec{r})}e^{i\theta(\vec{r})}, \tag{6.1}$$

including $\theta(\vec{r})$ as its phase. For *microscopic* wavefunctions, we would interpret ρ as a probability density. However, here we can interpret ρ as a particle density because it's the wavefunction of a large collection of Cooper pairs.

We postulate that the state $\psi(\vec{r})$ obeys the Schrödinger equation for a particle of charge q coupled to an electromagnetic field. The Hamiltonian for such a particle (written in the position representation) is well known to be

$$\hat{H} \equiv \frac{1}{2m}\left(\frac{\hbar}{i}\vec{\nabla} - q\vec{A}(\vec{r})\right)^2 + q\phi(\vec{r}), \tag{6.2}$$

where $\vec{A}(\vec{r})$ is the vector potential of the magnetic field and $\phi(\vec{r})$ the scalar potential of the electric field. From this point forward, we'll drop the explicit $\vec{r}$ dependence. In the full Ginzburg–Landau theory, there are nonlinear corrections to this basic Hamiltonian, which we ignore here. For a Cooper pair, we have that $q = 2e$, where e is the charge of the electron. We leave this constant general for now since the experimental determination of its value provided important evidence that the superconducting state involved pairs of electrons. Using the Schrödinger equation, we can then derive a conservation law for Cooper pairs (charge),

$$\frac{\partial}{\partial t}(\psi(\vec{r})^*\psi(\vec{r})) = -\vec{\nabla}\cdot\vec{J} = 0, \tag{6.3}$$

where $\vec{J}$ is the current describing the collective motion of the Cooper pairs,

$$\vec{J} = \frac{1}{2m}\left[\psi^*\left(\frac{\hbar}{i}\vec{\nabla} - q\vec{A}\right)\psi + \psi\left(-\frac{\hbar}{i}\vec{\nabla} - q\vec{A}\right)\hat{\psi}^*\right]. \tag{6.4}$$

These last two equations would each have the same form for a microscopic wavefunction but would be interpreted as a conservation law for *probability*. Using the ansatz, Eq. (6.1), we get the explicit form

$$\vec{J} = \frac{\hbar}{m}\left[\vec{\nabla}\theta - \frac{q}{\hbar}\vec{A}\right]\rho = \vec{v}\rho, \tag{6.5}$$

where in the last step we have defined $\vec{v} := \frac{\hbar}{m}[\vec{\nabla}\theta - \frac{q}{\hbar}\vec{A}]$. With the general observation that a particle current can be defined as the density of particles times their velocity, we can identify $\vec{v}$ as the velocity of the fluid of Cooper pairs, also known as the **condensate velocity**.

6.1.3 Magnetic Flux Quantization

An interesting and unique property of superconducting systems is that magnetic flux within a superconducting loop becomes quantized. This is a consequence of the superconducting

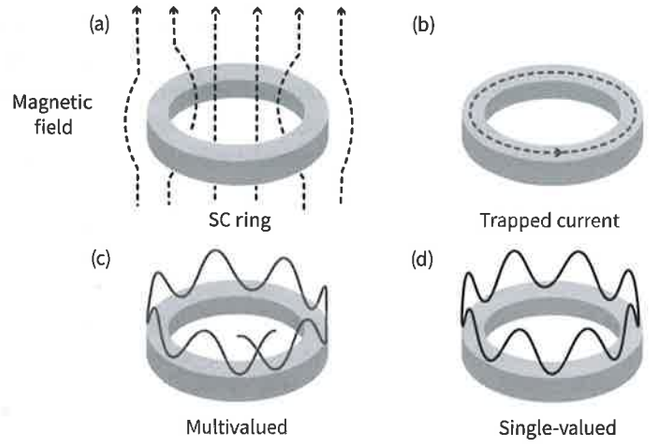

Fig. 6.3 **Magnetic flux quantum trapped in a superconducting ring.** (a) A superconducting ring in uniformly applied external field, $\vec{B}$, perpendicular to the plane of the ring. (b) The field will induce a current that travels along the surface of the ring. This current maintains the flux quantization by generating its own field that adds to or subtracts from the applied field. (c) For an arbitrary flux through the ring, the wavefunction would be multivalued, which is unphysical. (d) With an integer number of flux quanta in the ring, the wavefunction is single-valued.

condensate having a coherent global phase. We'll examine flux quantization here because it's a building block of many superconducting qubits.

We'll start by considering a superconducting ring that's threaded by a uniformly applied magnetic field, $\vec{B}$, oriented perpendicular to the plane of the ring (Fig. 6.3a). The Meissner effect implies a screening current develops on the surface of the superconductor that cancels the magnetic field in the bulk. (Experiments and detailed theory show this is the case.) Since the current density is zero deep inside our superconducting ring, i.e. $\vec{J} = 0$, it follows that

$$\vec{J} = \frac{\hbar}{m}\left[\vec{\nabla}\theta - \frac{q}{\hbar}\vec{A}\right]\rho = 0 \quad \Rightarrow \quad \vec{\nabla}\theta = \frac{q}{\hbar}\vec{A}. \tag{6.6}$$

We now take the line integral of both sides of this equation around a closed contour, Γ, that passes deep inside the superconducting ring, yielding

$$\oint_\Gamma \vec{\nabla}\theta\cdot\mathrm{d}\vec{l} = \frac{q}{\hbar}\oint_\Gamma \vec{A}\cdot\mathrm{d}\vec{l}. \tag{6.7}$$

We can simplify the right-hand side of this equation by applying **Stokes' theorem** ($\oint \vec{A}\cdot\mathrm{d}\vec{l} = \int_S(\vec{\nabla}\times\vec{A})\cdot\mathrm{d}\vec{S}$), where S is the surface enclosed by Γ, and the definitions of the vector potential ($\vec{\nabla}\times\vec{A} = \vec{B}$) and the magnetic flux ($\Phi = \int_S \vec{B}\cdot\mathrm{d}\vec{S}$), finding

$$\frac{q}{\hbar}\oint \vec{A}\cdot\mathrm{d}\vec{l} = \frac{q}{\hbar}\int_S(\vec{\nabla}\times\vec{A})\cdot\mathrm{d}\vec{S} = \frac{q}{\hbar}\int_S \vec{B}\cdot\mathrm{d}\vec{S} = \frac{q\Phi}{\hbar}. \tag{6.8}$$

For the left-hand side, we can start again with a result from vector calculus:

$$\int_1^2 \vec{\nabla}\theta\cdot\mathrm{d}\vec{l} = \theta_2 - \theta_1, \tag{6.9}$$

which would be zero for a closed contour if the field (phase) were simply connected. In a multiply connected field, like the superconducting phase of our ring, it doesn't need to be. To go further, we must add a *physical* requirement, which is that the wavefunction of the superconductor is single-valued at any point in space and time. That is, if the phase starts with a value θ_0, once you return to the initial point, the phase can only take on values of $\theta_0 = \theta_0 + 2n\pi$. Otherwise, the wavefunction would have a different value, as depicted in Fig. 6.3c. This then implies

$$\oint_\Gamma \vec{\nabla}\theta \cdot \mathrm{d}l = 2\pi n, \tag{6.10}$$

where $n \in \mathbb{Z}$. Thus we find that the flux through the ring is equal to

$$\Phi = \frac{2\pi\hbar}{q} n = \Phi_0 n, \tag{6.11}$$

where $q = 2e$ and we defined $\Phi_0 := \frac{\pi\hbar}{e} = \frac{h}{2e}$ where h is Planck's constant. That is, the flux through the ring is quantized, taking on values that are integer multiples of Φ_0. Φ_0 is known as the superconducting **flux quantum**. Physically, this flux quantization is enforced by the screening current that flows in the superconducting ring, either adding or subtracting the appropriate amount of flux.

6.2 Superconducting Circuits

Equipped with this brief introduction to superconductivity, we can now consider superconducting circuits. We'll first describe some of the desired properties of an artificial atom needed to build a qubit (Section 6.2.1). We'll then try to build the qubit with a superconducting LC circuit. To do so, we'll first present the classical LC circuit in Section 6.2.2. Using the canonical quantization procedure, we'll then find the Hamiltonian for the quantized LC circuit in Section 6.2.3. However, we'll find that to build an artificial atom we will require a nonlinear circuit element. The nonlinear element of choice in superconducting quantum computing is the Josephson junction, which we introduce in Section 6.2.4. Finally, in Section 6.2.5 we introduce a type of tunable Josephson junction known as a DC-SQUID.

6.2.1 Artificial Atom

First, let's outline our criteria for building an "artificial atom" for quantum computing. This is a system with an energy spectrum that is discrete, well-separated, and anharmonic. For our first criterion, we need a Hamiltonian with a discrete spectrum, like a natural atom. For our second criterion, we need the separation between adjacent energy levels to be much larger than both the thermal fluctuations of the environment and any broadening of the levels induced by coupling to the environment. (Small broadening implies weak coupling to the environment.) Our third criterion, an anharmonic spectrum, is helpful for controlling the qubit using Rabi oscillations or similar techniques. Consider a system that has a harmonic (i.e. equidistant) spectrum, that is, $\Delta E = E_1 - E_0 = E_2 - E_1 = \cdots$, where E_n is the energy

of the nth energy level. Now, assume that we'd like to excite the system from its ground state to its first excited state. As we've seen many times in this text, we can do so by driving the system resonantly at $\omega_{01} = (E_1 - E_0)/\hbar$. However, this is also the transition frequency to the next level, and so forth. Thus, we would end up exciting the system to a superposition of many energy levels. We avoid this outcome by making the levels anharmonic. These three properties are characteristic of the spectrum of natural atoms, which is why we call superconducting qubits "artificial atoms." Once built, our artificial atom will be a multilevel system, but we will encode our qubit in two of its energy levels, typically the two lowest.

Given that classical computers are built with electronic circuits, it's reasonable to contemplate quantum electronic circuits to build quantum computers. In the next section we'll first consider one of the simplest circuits, an LC oscillator. We'll find that a superconducting LC oscillator can satisfy our first two criteria for an artificial atom, but fails to satisfy the requirement of anharmonicity. To achieve anharmonicity, we'll need to introduce a nonlinear circuit element: the Josephson junction.

6.2.2 Classical LC Oscillator

The two components of an LC oscillator are an **inductor** and a **capacitor**, which are characterized by their **inductance**, L, and **capacitance**, C. A typical inductor consists of a current-carrying wire that's been shaped into a coil. When a current moves through the inductor, it induces a magnetic field in the inductor. Importantly, this magnetic field stores energy, often referred to as **inductive energy**. The inductance, L, is defined by the relation between the current in the inductor, I, and the magnetic flux through the inductor, Φ. The flux is given by the integral of the magnetic field over the cross-section S of the inductor's coil, i.e. $\Phi = \int_S \vec{B} \cdot \mathrm{d}\vec{S}$. In detail, we have that

$$L = \frac{\Phi}{I}. \tag{6.12}$$

Combining this definition with Faraday's law of induction, we arrive at the so-called **constitutive relation** for the inductor, which relates I to the voltage V across the coil: $V = L\frac{\mathrm{d}I}{\mathrm{d}t}$. In the context of superconducting quantum circuits, we will often find it convenient to use the less-conventional integral form of this relation,

$$\Phi(t) = \int_{-\infty}^{t} V(t')\mathrm{d}t', \tag{6.13}$$

where it's assumed that at time $t = -\infty$ the circuit is at rest with no stored energy.

A typical capacitor consists of two conducting plates separated by an insulating region, which can be a vacuum or dielectric material. A voltage applied to a capacitor will cause opposite charges to build up on the plates of the capacitor, producing an electric field in the insulating region. Complementary to the inductive energy above, this electric field also stores energy, commonly referred to as the **charging energy**. In fact, a capacitor can be seen as an electromagnetic dual of an inductor in many ways. Gauss' law generally relates the charge on the capacitor to the electric field through $Q = \epsilon_0 \oint_S \vec{E} \cdot \mathrm{d}\vec{S}$ where, in this case, S is a closed surface containing one of the capacitor plates. For the simplified

geometry of a parallel plate capacitor, $|\vec{E}|$ is approximately uniform between the plates and negligible outside of them, and Gauss' law reduces to $Q = \epsilon_0 |\vec{E}| a$, where a is the area of the capacitor plates. Further, from the definition of electrical potential, we have that the voltage (potential difference) between the plates is the line integral of E, which for parallel plates gives $V = E/d$, where d is the separation of the plates. Putting this together, we get

$$C = \frac{Q}{V}, \tag{6.14}$$

where the capacitance, C, is the constant relating Q and V. For a parallel-plate capacitor this reduces to $C = \epsilon_0 a/d$. Due to the linearity of Maxwell's equations, this linear relation between Q and V holds for a general geometry, even if the exact expression for C will depend on the specific geometry. The charge $Q(t)$ on the conductor is given by the conservation of charge,

$$Q(t) = \int_{-\infty}^{t} I(t')\mathrm{d}t', \tag{6.15}$$

where $I(t)$ is the current flowing to the capacitor. Combining the differential of this relation with Eq. (6.14) yields the constitutive relation for the capacitor: $I = C\frac{\mathrm{d}V}{\mathrm{d}t}$.

As we mentioned, inductors and capacitors store energy. This energy can be found by taking the integral of the power

$$E = \int_{-\infty}^{t} P(t)\mathrm{d}t = \int_{-\infty}^{t} V(t)I(t)\mathrm{d}t, \tag{6.16}$$

where we used **Watt's law**, $P(t) = V(t)I(t)$. Importantly, ideal capacitors and inductors are considered to be lossless elements, meaning that all energy put into them can be extracted. This is in contrast to a dissipative element like a resistor. We can write the energy of the capacitor and inductor in terms of the flux and charge. For the inductor, we find

$$E_{\mathrm{L}}(t) = \int_{-\infty}^{t} V(t')I(t')\mathrm{d}t' = \int_{-\infty}^{t} \left(L\frac{\mathrm{d}I(t')}{\mathrm{d}t'}\right) I(t')\mathrm{d}t' = \frac{LI^2}{2} = \frac{\Phi^2}{2L}, \tag{6.17}$$

and for the capacitor, we find

$$E_{\mathrm{Cap}}(t) = \int_{-\infty}^{t} V(t')I(t')\mathrm{d}t' = \int_{-\infty}^{t} V(t')\left(C\frac{\mathrm{d}V(t')}{\mathrm{d}t'}\right)\mathrm{d}t' = \frac{CV^2}{2} = \frac{Q^2}{2C}. \tag{6.18}$$

We will now find the classical Hamiltonian of this circuit by following the standard prescription of classical mechanics. That is, we will start by writing down the Lagrangian[3] of the circuit and then derive the Hamiltonian using the Legendre transformation after deriving the canonical variables of the circuit. In standard (classical) circuit analysis, we typically work with the dynamical variables I and V. In the context of the Lagrangian and Hamiltonian formalisms, we will find it instead better to work with Φ and Q, as explained

[3] As a brief note on interpretation for those who are unfamiliar with Lagrangian and Hamiltonian formalisms, in classical mechanics they are advanced methods for solving the dynamics of complex coupled systems. We start by writing the Lagrangian in terms of the uncoupled circuit variables of the individual components. We then derive the canonical variables, which can be seen as the "true" degrees of freedom of the coupled circuit, including constraints imposed by the circuit topology, i.e. Kirchoff's laws. Finally, we write the Hamiltonian, which essentially expresses the system's energy, in terms of these true degrees of freedom.

below. In this context, Eq. (6.13) can be taken to define the flux, Φ, across any circuit element or at any circuit node as the time integral of the voltage across it. In this general context, the circuit variable Φ no longer has the literal meaning of magnetic flux, but it is, nonetheless, perfectly well defined. Finally, we remark that the Lagrangian and Hamiltonian formalisms are a somewhat heavy-handed approach for a circuit as simple as the LC oscillator, but the following derivation illustrates the formalism, which will be useful for more complex circuits.

In classical mechanics, the Lagrangian is taken to be a functional of the kinetic energy, $\mathcal{T}$, and potential energy, $\mathcal{V}$, of the system. We must then choose which roles our capacitive and inductive energies will play in our electrical analogue. The choice is arbitrary in general, but we will find it convenient in superconducting circuits to assign the energy of the capacitor to $\mathcal{T}$ and the energy of the inductor to $\mathcal{V}$. This is equivalent to choosing the flux to play the role of position and the charge the role of momentum. The Lagrangian is thus,

$$\mathcal{L} = \mathcal{T} - \mathcal{V} = \frac{1}{2}C\dot{\Phi}^2 - \frac{1}{2L}\Phi^2. \tag{6.19}$$

(The over-dot is a commonly used notation for the time derivative.) Next, we find the so-called canonically conjugate momentum, $\mathcal{P}$, to the coordinate Φ:

$$\mathcal{P} \coloneqq \frac{\partial \mathcal{L}}{\partial \dot{\Phi}} = C\dot{\Phi} = Q. \tag{6.20}$$

In the case of this simple circuit, the canonical momentum is the charge on the capacitor. In general, it will be a more complicated function of multiple circuit variables, although maintaining units of charge. We can now obtain the Hamiltonian using the Legendre transformation

$$H_{\mathrm{LC}} \coloneqq \mathcal{P}\dot{\Phi} - \mathcal{L} = \frac{Q^2}{2C} + \frac{\Phi^2}{2L}, \tag{6.21}$$

which is the expected form of the energy of an LC circuit. Note that we expressed the Hamiltonian only in terms of the canonical variables, Q and Φ; other variables, such as $\dot{\Phi}$, must be eliminated in the final expression.

We can recognize Eq. (6.21) as the Hamiltonian for the harmonic oscillator. When an inductor is connected to a charged capacitor, the circuit's energy will oscillate between the two components via simple harmonic oscillations. The voltage across the capacitor will drop to zero as it drives a current through the inductor, causing the inductor to build up a magnetic field (Fig. 6.4). As per Faraday–Lenz's law, this magnetic field will induce a voltage in the inductor's coil that opposes the current flow, eventually reversing the current. The energy stored in the inductor will thus fall to zero as it recharges the capacitor with the opposite polarity. This cycle repeats, with the energy in the LC circuit oscillating between the two components with a frequency

$$\omega_r = \frac{1}{\sqrt{LC}}. \tag{6.22}$$

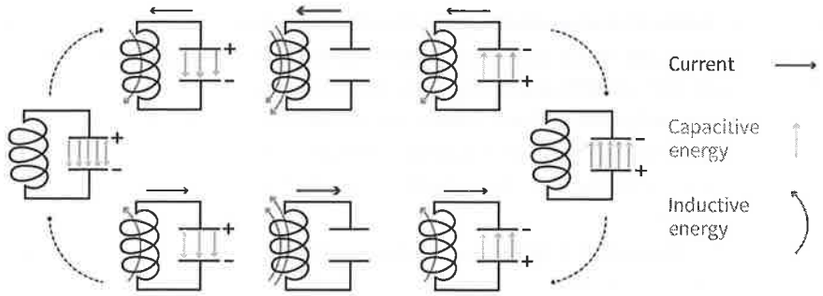

Fig. 6.4 **Energy oscillating in an LC circuit.** The voltage across the charged capacitor drives a current through the inductor, causing the inductor to build up a magnetic field. The current continues to flow in the same direction until the charge on the capacitor has flipped and the current then stops. The process then begins again with the current flowing in the opposite direction.

6.2.3 Quantized LC Oscillator

We will quantize our LC oscillator in the same way we did for the harmonic oscillator in Section 2.6, that is, by following the procedure of canonical quantization. Since Φ and Q are canonically conjugate variables, we quantize our Hamiltonian by promoting these variables to operators,

$$Q \to \hat{Q}, \quad \Phi \to \hat{\Phi}, \tag{6.23}$$

and imposing the commutation relation

$$\left[\hat{\Phi}, \hat{Q}\right] = i\hbar. \tag{6.24}$$

Here we see an intuitive motivation for using Φ and Q as our canonical circuit variables, instead of I and V: They have the correct units such that their commutator has the same units as $\hbar$.

We can now express our Hamiltonian *operator* as

$$\hat{H}_{\mathrm{LC}} = \frac{1}{2C}\hat{Q}^2 + \frac{C\omega_r^2}{2}\hat{\Phi}^2. \tag{6.25}$$

We used the definition of ω_r to write the Hamiltonian in terms of C to highlight how, in our circuit analogy, C plays the role of mass. This is consistent with our choice to associate the capacitive energy with the kinetic energy.

Now that we have expressed the circuit Hamiltonian in the form of a quantum harmonic oscillator, we can solve the system as we have done previously. We start by defining the ladder operators,

$$\hat{\Phi} = \Phi_{\mathrm{zpf}}(\hat{a}^\dagger + \hat{a}) \quad \text{and} \quad \hat{Q} = iQ_{\mathrm{zpf}}(\hat{a}^\dagger - \hat{a}), \tag{6.26}$$

where $\Phi_{\mathrm{zpf}} := \sqrt{\hbar Z_r/2}$ and $Q_{\mathrm{zpf}} := \sqrt{\hbar/2Z_r}$ are the **zero-point fluctuations** of the flux and charge, respectively, and $Z_r = \sqrt{L/C}$ is the characteristic impedance of the oscillator.

The creation operator $\hat{a}^\dagger = \sqrt{1/2\hbar Z_r}(\hat{\Phi} - iZ_r\hat{Q})$ thus creates an excitation of the oscillator of frequency ω_r. The Hamiltonian of the LC oscillator thus takes the usual form

$$\hat{H}_{\mathrm{LC}} = \hbar\omega_r\left(\hat{a}^\dagger\hat{a} + \frac{1}{2}\right). \tag{6.27}$$

Usually, we think of quantum systems as being very small, of atomic scale, but the Hamiltonian $\hat{H}_{\mathrm{LC}}$ can describe any scale. The validity of the quantization procedure for a mesoscopic or even macroscopic system can be viewed as a hypothesis, but one that has been extensively tested and verified with a high degree of precision. At the same time, a theoretical motivation for this procedure is that the constitutive relations governing the inductor and capacitor have been derived directly from Maxwell's equations, and these relations serve as a convenient tool for calculating the behaviour of the electromagnetic field in the presence of conductors and dielectrics. In that sense, what is really being quantized in Eq. (6.25) is the electromagnetic field itself.

One way of choosing the scale of our superconducting quantum devices is by choosing the frequency ω_r. By choosing the right frequency for our circuit, we can ensure the separation between energy levels is much greater than the thermal energy, i.e. $\hbar\omega_r \gg k_B T$. Thus, the temperature that can practically be achieved sets a lower bound on ω_r. For scale, a frequency of 10 GHz corresponds to a temperature of about 480 mK. In practice, we want the thermal energy to be several times smaller than the energy spacing so that the thermal excitation probability is negligible. In a modern dilution refrigerator with state-of-the-art filtering, it's possible to cool the circuit below $T \sim 20$ mK. All this together implies a minimum operating frequency of a few gigahertz.

There exist some upper bounds on ω_r too. First, if the frequency is too high, the excitation of the resonator will have sufficient energy to break Cooper pairs, and the system will not function as a superconductor. This implies that we want $\omega_r \ll \Delta_{\mathrm{BCS}}/\hbar$. In aluminum, for example, $\Delta_{\mathrm{BCS}}/h \sim 50$ GHz. (In fact, the energy to break a Cooper pair is $2\Delta_{\mathrm{BCS}}$, sometimes called the spectroscopic gap.) Other common superconductors, such as niobium, have much higher gaps. However, there is a technological challenge in pushing operation to the terahertz range, ~0.1–10 THz, between optical and microwaves, as the technologies for generating and detecting radiation are inefficient and impractical. Thus we're bounded from above by $\omega \sim 100$ GHz.

In practice, most superconducting qubit systems operate approximately in the range of 5–10 GHz, which fits nicely in the bounds above. This range also overlaps with the frequency bands of many important communication protocols, such as LTE for cellphones and Wi-Fi for computing, allowing superconducting quantum devices to exploit a large amount of already existing technology.

6.2.4 Josephson Junction

Our method to build a qubit is finding a quantum system with good control of two of its states. In superconducting systems, the control is through coherent fields similar to NMR. Unfortunately, a superconducting LC circuit behaves as a harmonic oscillator, and our control cannot isolate only two levels as they all have the same spacing. We need to add

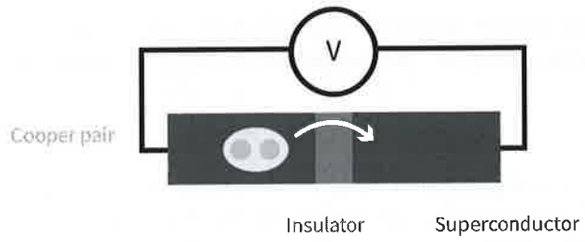

Fig. 6.5 **Josephson junction.** A Josephson junction consists of two superconductors separated by a thin insulator. Cooper pairs will cross the insulator via the effect of quantum tunnelling. This tunnelling causes the junction to have an inductive energy; thus, it operationally behaves like a nonlinear inductor.

some anharmonicity from a nonlinear circuit element with very low dissipation to our quantum system.

While there are many types of superconducting qubits, the **Josephson junction** (Fig 6.5) is the nonlinear element of choice in qubit design. The Josephson junction is named after Brian Josephson, who first predicted the existence of a supercurrent for these devices while still a Ph.D. candidate. He received the Nobel Prize for his work in 1973. The most common form of a Josephson junction is a **tunnel junction** with two superconducting electrodes. It is a device built from two conductors separated by an insulating barrier. Classically, electrons can't cross the insulating barrier. However, quantum mechanics allows electrons to tunnel through the barrier. We can control the probability of tunnelling by adjusting, for example, the insulator's thickness or the insulator's type, which determines the height of the energy barrier. More generally, a Josephson junction can be formed by any "weak link" between two superconductors. In a typical tunnel junction, the probability of an electron impinging on the barrier tunnels is very small, in the range $p \sim 10^{-5}$–10^{-6}. Before Josephson, it was assumed that the probability of a Cooper pair tunnelling would be $\sim p^2$, implying that any superconducting current through the junction would be negligible. Contrary to these expectations, Josephson predicted that, due to the phase coherence between electrons, Cooper pairs tunnel with probability $\sim p$, just like single electrons in a normal-metal tunnel junction.

Josephson further derived a pair of constitutive equations, now known as the **Josephson equations**, that describe the dynamics of a Josephson junction in terms of the current and voltage across it. These elements' nonlinearity is needed to build a superconducting qubit. Josephson's derivations of the Josephson equations are beyond the scope of this textbook. In that derivation, Josephson used microscopic tunnelling theory while accounting for the superconducting electrodes' quantum coherence. Here, we will motivate the Josephson equations using a phenomenological approach, due to Feynman, based on the macroscopic wavefunction concept we introduced above.

To motivate the Josephson equations, we start by writing down a minimal model (Schrödinger equation) for coupled electrodes:

$$i\hbar\frac{\partial\psi_1}{\partial t} = E_1\psi_1 + K\psi_2 \quad \text{and} \quad i\hbar\frac{\partial\psi_2}{\partial t} = E_2\psi_2 + K\psi_1, \tag{6.28}$$

where ψ_i is the superconducting wavefunction of electrode i, E_i is the self-energy (chemical potential) of electrode i, and K is a coupling constant (tunnelling amplitude) that's determined by the tunnel barrier. The second term of each equation is often called the tunnelling term, as it represents the tunnelling of Cooper pairs between the electrodes. If we now imagine applying a voltage V across the electrodes, then the energy difference between the two superconductors is $E_1 - E_2 = 2eV$, since each Cooper pair has charge $q = 2e$.

By substituting the ansatz wavefunction, Eq. (6.1), into the Schrödinger equation for the electrodes, Eq. (6.28), we find that the time evolution of the density and phase of the wavefunction in each electrode is

$$\dot{\rho}_1 = +\frac{2}{\hbar}K\sqrt{\rho_1\rho_2}\sin(\phi), \tag{6.29}$$

$$\dot{\rho}_2 = -\frac{2}{\hbar}K\sqrt{\rho_1\rho_2}\sin(\phi), \tag{6.30}$$

$$\dot{\theta}_1 = -\frac{K}{\hbar}\sqrt{\frac{\rho_2}{\rho_1}}\cos(\phi) - \frac{eV}{\hbar}, \tag{6.31}$$

$$\dot{\theta}_2 = -\frac{K}{\hbar}\sqrt{\frac{\rho_1}{\rho_2}}\cos(\phi) + \frac{eV}{\hbar}, \tag{6.32}$$

where $\phi := \theta_2 - \theta_1$ is the superconducting phase difference. We see from the first pair of equations that $\dot{\rho}_1 = -\dot{\rho}_2$, i.e. as we expect from charge conservation. Thus the current across the junction is

$$I = c\dot{\rho}_1 = \frac{2cK}{\hbar}\sqrt{\rho_1\rho_2}\sin(\phi) = I_c\sin(\phi), \tag{6.33}$$

where c is a constant of proportionality and we defined $I_c := \frac{2cK}{\hbar}\sqrt{\rho_1\rho_2}$. This is known as the **first Josephson equation**. It gives the current from the Cooper pairs tunnelling across the junction as a function of the macroscopic phase difference between the electrodes. I_c is the critical current, the maximum current that can flow before the Cooper pairs break and superconductivity is lost. We also frequently encounter the related critical current density, $J_c = I_c/A$, where A is the area of the tunnel junction. The magnitude of the critical current is determined by the tunnel barrier and the material properties of the electrodes. Microscopic calculations, due to Vinay Ambegaokar and Alexis Baratoff, show $I_c = \pi\Delta_{\text{BCS}}/2R_ne$, where Δ_{BCS} is the superconducting energy gap of the electrodes and R_n is the normal-state resistance of the tunnel junction. That is, R_n is the Ohmic resistance of the tunnel junction when both electrodes are in the normal-metal state. It gives us a phenomenological measure of the strength of the tunnelling.

We can now find a relationship between the rate of change of the phase difference across the junction and the voltage across the junction by combining Eqs. (6.31) and (6.32). In doing so, we find

$$\dot{\phi} = \dot{\theta}_2 - \dot{\theta}_1 = \frac{2e}{\hbar}V = \frac{2\pi}{\Phi_0}V, \tag{6.34}$$

where we have assumed that ρ_1 and ρ_2 are approximately constant and equal. Assuming they're constant is a good approximation so long as the effect of tunnelling is small. Moreover, they are equal when we use the same metal on both sides of the junction.

This relationship is known as the **second Josephson equation**. By integrating over the second Josephson equation, we also find that the superconducting phase difference, ϕ, is proportional to the flux across the junction,

$$\phi = \int_{-\infty}^{t} \dot{\phi} \mathrm{d}t' = \frac{2\pi}{\Phi_0} \int_{-\infty}^{t} V(t') \mathrm{d}t' = \frac{2\pi}{\Phi_0} \Phi, \tag{6.35}$$

where in the last step we used Eq. (6.13) to get the result that $V = \frac{\mathrm{d}\Phi}{\mathrm{d}t}$ and assume an initial condition $V(t = -\infty) = 0$.

Using the Josephson equations, we can demonstrate that the inductance of a Josephson junction is nonlinear with respect to Φ. To do so, we first substitute the first Josephson equation and the second Josephson equation into the definition for inductance,

$$L = V \left(\frac{\mathrm{d}I}{\mathrm{d}t} \right)^{-1} = \frac{V}{I_c} \left(\frac{\mathrm{d} \sin(\phi)}{\mathrm{d}t} \right)^{-1} = \frac{V}{I_c \dot{\phi} \cos\phi} = \frac{V \Phi_0}{2\pi V I_c \cos\phi} = \frac{L_{J_0}}{\cos\phi}, \tag{6.36}$$

where we define $L_{J0} = \Phi_0/(2\pi I_c)$, which is known as the **Josephson inductance**. Then, by substituting the definition of ϕ into the equation for the inductance, we find

$$L_J(\Phi) = L_{J0} \frac{1}{\cos(2\pi \Phi/\Phi_0)}. \tag{6.37}$$

Thus the Josephson junction has an inductance which is nonlinear with respect to the flux, with a linearized value of L_{J0}.

We can also find the energy stored in a Josephson junction. We assume the junction starts from rest with $\phi = 0$ at $t = 0$. We can then find the energy at a later time, t, by again using Watt's law and integrating the power $P = IV$. By substituting the first and second Josephson equations into this equation, we find

$$E = \int_0^t I(t')V(t')\mathrm{d}t' = \frac{I_c \Phi_0}{2\pi} \int_0^{\phi} \sin(\phi')\mathrm{d}\phi' = E_J \left(1 - \cos(\phi)\right), \tag{6.38}$$

where $E_J = \Phi_0 I_c/2\pi$ is known as the **Josephson energy**.

6.2.5 DC-SQUID

An interesting and useful feature of engineered qubits is that they can have a high degree of *in situ* tunability.[4] We can take advantage of this tunability to implement gates more quickly and with higher fidelity. For example, as we will see when we perform a two-qubit gate, we will at times want to bring two qubits into resonance with one another for some period of time and then take them out of resonance.

In superconducting qubits, this tunability is frequently enabled by replacing a simple Josephson junction by a related device known as a DC-SQUID (superconducting quantum interference device). The DC-SQUID effectively makes a Josephson junction with a value of I_c that can be tuned with a magnetic field. The SQUID consists of two Josephson junctions put in parallel to form a ring. Referring to Fig. 6.7, a Cooper pair entering on the left

[4] This is a tunability which is possible after the system has been fabricated.

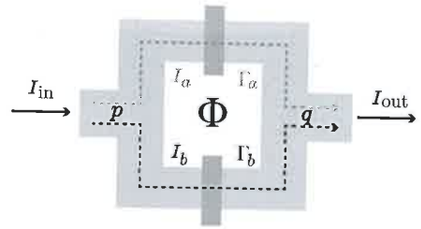

Fig. 6.6 **DC superconducting quantum interference device (DC-SQUID).** A DC-SQUID consists of two Josephson junctions connected in parallel to form a loop. A DC-SQUID operates like a Josephson junction whose Josephson energy can be tuned after it's fabricated, by adjusting the flux through the SQUID's loop.

has two choices, going through path a or b, leading to the potential interference of the superconducting phases

$$\Delta\theta_a = \delta_a + \frac{2e}{\hbar} \int_{p\to q}^{\text{up}} \vec{A} \cdot \mathrm{d}\vec{l} \;\; ; \;\; \Delta\theta_b = \delta_b + \frac{2e}{\hbar} \int_{p\to q}^{\text{down}} \vec{A} \cdot \mathrm{d}\vec{l}, \tag{6.39}$$

where $\vec{A}$ is the vector potential associated with the flux Φ, and δ_a (δ_b) is the phase difference across junction a (b). So that the Cooper pair wavefunction is single-valued, we physically require these two phases to be the same, i.e. $\Delta\theta_a = \Delta\theta_b$, which leads to

$$\delta_b - \delta_a = \frac{2e}{\hbar} \oint_{\Gamma} \vec{A} \cdot \mathrm{d}\vec{l} = \frac{2e}{\hbar} \Phi = 2\pi \frac{\Phi}{\Phi_0}. \tag{6.40}$$

The total current across the circuit is then

$$I_{\text{total}} = I_0[\sin\delta_a + \sin\delta_b] = I_0 \sin\frac{1}{2}(\delta_a + \delta_b) \cos\frac{1}{2}(\delta_a - \delta_b) \tag{6.41}$$

$$= I_0 \cos\left(\pi \frac{\Phi}{\Phi_0}\right) \sin\delta \tag{6.42}$$

$$= I_C(\Phi) \sin\delta, \tag{6.43}$$

where we have defined $\delta = (\delta_a + \delta_b)/2$. We see that this indeed looks like a Josephson junction that can be tuned by the flux Φ.

6.3 Qubit

With all the ingredients in hand, we can now introduce one of the first superconducting qubits, the **Cooper-pair box** (CPB) (Section 6.3.1). The derivation of its properties as a qubit is relatively straightforward and serves as a pedagogical application of circuit quantization. However, the CPB is generally no longer used as a qubit because it is highly susceptible to environmental charge noise. We will then introduce an alternative qubit design which is more resistant to charge noise: the transmon (Section 6.3.2). It has the same basic Hamiltonian as the CPB, but is designed with very different parameters. We'll conclude this

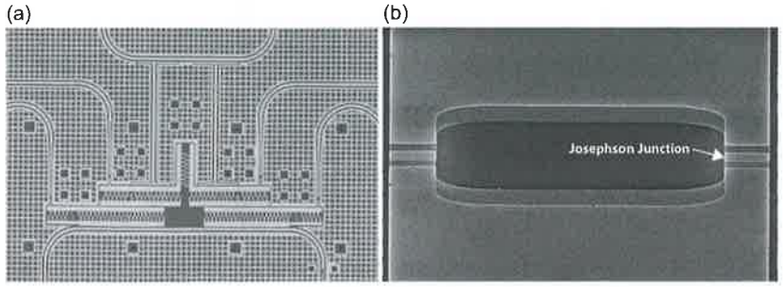

Fig. 6.7 **Micrographs of superconducting quantum devices.** (a) A micrograph of a small superconducting quantum processor with four transmon qubits (see Section 6.3.2). The brighter areas are aluminum and the darker areas are the silicon substrate below. The transmons are the structures with "teeth," that is, interdigitated capacitors that form the shunt capacitors of the transmons. The solid aluminum lines and the surrounding ground planes, which are perforated with square holes, form microwave waveguides (see Section 6.4.2). The pitch of the squares is about 20 μm. (b) An electron micrograph of a SQUID. The center of the SQUID loop is the center of the micrograph. The Josephson junctions, symmetrically placed in the vertical center of the image, are formed by the overlap of two aluminum layers. The height of the junctions is about 300 nm.

section with a brief discussion of two other prominent types of superconducting qubits in Section 6.3.4.

6.3.1 Cooper–Pair Box

The CPB is the canonical example of a **charge qubit**. We will first introduce the Hamiltonian of the general charge qubit. We'll then consider different regimes of this Hamiltonian, one of which describes the CPB.

Hamiltonian

So far, we have considered an idealized notion of a Josephson junction in which they are solely nonlinear inductors. However, as one might expect from their physical resemblance to capacitors, Josephson junctions based on tunnel junctions always have a parasitic capacitance. Thus, we take the model of a physical Josephson junction to consist of an "ideal Josephson element" that's connected in parallel to a capacitor, C_J, as shown in Fig. 6.8.

Charge qubits are a family of superconducting qubits which have a similar circuit design. This circuit consists of a gate capacitor, C_g, connected in series with a Josephson junction, as shown in Fig. 6.9a. We label a portion of this circuit as the **island** and another portion as the **reservoir**. As seen from Fig. 6.9a, the island is a piece of superconducting material that is physically separated from the rest of the circuit by a spatial gap and by an insulator. The conductor that is separated from the island by the insulator is known as the reservoir, implying that it is physically much larger, and we assume that its state is not affected by the tunnelling of Cooper pairs on to, or off of, the island.

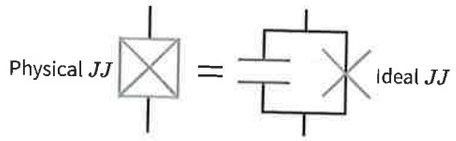

Fig. 6.8 **Physical and ideal Josephson junction.** A physical Josephson junction consists of an ideal Josephson junction with a small parasitic capacitor connected in parallel. The capacitor represents the geometric capacitance of the Josephson junction's electrodes.

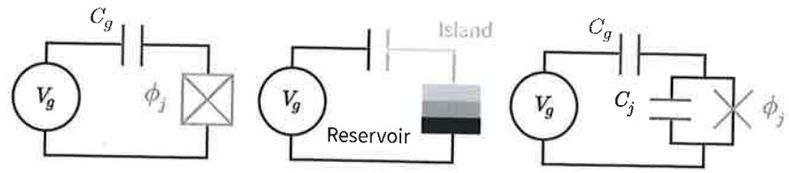

(a) Circuit with physical JJ (b) The island (c) Circuit with ideal JJ

Fig. 6.9 **Charge qubit.** (a) A charge qubit consists of a voltage source, a gate capacitor C_g, and a Josephson junction. (b) The island is a small piece of metal defined from the empty space in C_g to the insulator in the Josephson junction. The reservoir is the other electrode of the Josephson junction that's not a part of the island, generally assumed to be a larger piece of metal. (c) This is the final circuit model of the CPB, including the ideal Josephson junction and its parasitic capacitance, C_j.

As with the LC circuit, we'll find the charge qubit Hamiltonian by using basic circuit analysis and Lagrangian mechanics applied to Fig. 6.9c. Introductory texts on circuit analysis will often introduce two equivalent methods to solve circuits: the node-voltage method and the loop-current method. In the quantum context, if the only nonlinear elements in our circuit are inductive elements, e.g. Josephson junctions, it is better to use the node-voltage method. In the node-voltage method, we start by identifying one particular node of the circuit as "ground," which we take to be the zero of the electrical potential. All other **node voltages**, and therefore fluxes, are then expressed relative to the ground. The voltages across individual elements, known as **branch voltages**, are then the differences of node voltages.

Referring to Fig. 6.9c, we will take the common node between the voltage source and the Josephson junction as the ground. We will then denote the flux of the island as Φ_J and the flux of the node between the voltage source and C_g as Φ_g. Since there are no other inductive elements in the circuit, the potential energy in our circuit is the energy of the Josephson junction,

$$\mathcal{V} = -E_j \cos\left(\frac{2\pi}{\Phi_0}(\Phi_J - 0)\right) = -E_j \cos\left(\frac{2\pi}{\Phi_0}\Phi_J\right). \tag{6.44}$$

We include the -0 in the first step to remind us that the Josephson energy is a function of the phase (flux) *difference* across it, even if we happen to have chosen one side of the junction as the ground node. Next, we write down the kinetic energy of the circuit as the

sum of the energies of all the capacitors,

$$\mathcal{T} = \frac{C_J}{2}(\dot{\Phi}_J - 0)^2 + \frac{C_g}{2}(\dot{\Phi}_J - \dot{\Phi}_g)^2 = \frac{C_J}{2}\dot{\Phi}_J^2 + \frac{C_g}{2}(\dot{\Phi}_J - V_g)^2. \tag{6.45}$$

In the second step, we approximate the voltage source as ideal, which imposes that $\dot{\Phi}_g = V_g$, introducing the classical control voltage V_g into the problem. Finally, our Lagrangian is

$$\mathcal{L} = \mathcal{T} - \mathcal{V} = \frac{C_J}{2}\dot{\Phi}_J^2 + \frac{C_g}{2}(\dot{\Phi}_J - V_g)^2 + E_J \cos\left(\frac{2\pi}{\Phi_0}\Phi_J\right). \tag{6.46}$$

Next, we'll use the Lagrangian to find the Hamiltonian. To do so, we first need to calculate the canonical momentum conjugate to Φ_J, which is the canonical charge

$$Q = \frac{\partial \mathcal{L}}{\partial \dot{\Phi}_J} = C_J\dot{\Phi}_J + C_g(\dot{\Phi}_J - V_g) = C_\Sigma\dot{\Phi}_J - C_g V_g, \tag{6.47}$$

where $C_\Sigma = C_g + C_J$. As mentioned previously, we see that in this case, the canonical charge has a more complicated form than the charge on any individual capacitor, reflecting the constraints imposed by the circuit topology. We also note that this canonical charge can be interpreted as the charge on the island of the CPB. We now calculate the Hamiltonian as

$$\begin{aligned} H &= Q\dot{\Phi}_J - \mathcal{L} \\ &= C_\Sigma\dot{\Phi}_J^2 - C_g V_g\dot{\Phi}_J - \frac{C_J}{2}\dot{\Phi}_J^2 - \frac{C_g}{2}(\dot{\Phi}_J - V_g)^2 - E_J\cos\left(\frac{2\pi}{\Phi_0}\Phi_J\right) \\ &= \frac{C_\Sigma\dot{\Phi}_J^2}{2} - E_J\cos\left(\frac{2\pi}{\Phi_0}\Phi_J\right), \end{aligned} \tag{6.48}$$

where in the last line we dropped the term $-C_g V_g^2/2$ because it does not contribute to the dynamics of the system. The final step in the process is to express the Hamiltonian only in terms of canonical variables, substituting $\dot{\Phi}_J = (Q + C_g V_g)/C_\Sigma$. By doing so, and promoting Q and Φ to quantum operators, we find the Hamiltonian of the charge qubit to be

$$\hat{H} = \frac{(\hat{Q} + C_g V_g)^2}{2C_\Sigma} - E_J\cos\left(\frac{2\pi}{\Phi_0}\hat{\Phi}\right). \tag{6.49}$$

We can now write the Hamiltonian in a more standard form by making a series of definitions and substitutions. First, we would like to work in terms of the number of Cooper pairs instead of the charge and in terms of the Josephson phase instead of the flux. To do so, we introduce the **Cooper-pair number operator**, $\hat{n}$ (beware, this is not the harmonic oscillator number operator), and the **phase difference operator**, $\hat{\phi}$. The operator $\hat{n}$ relates to the number of Cooper pairs that have tunnelled across the junction; in other words, the *excess* number of Cooper pairs on the island. The operator $\hat{\phi}$ relates to the superconducting phase difference across the junction. Importantly, because these operators relate to the differences of node variables across the junction, they are *branch* operators and not *node* operators, which introduces some subtleties. For our particular choice of

ground, we can write $\hat{n} := -\hat{Q}/2e$ and $\hat{\phi} := 2\pi\hat{\Phi}/\Phi_0$. Second, we define the **gate charge** as $n_g := Q_g/2e = C_g V_g/2e$, which is controlled by the classical voltage bias. Finally, we define the **charging energy** as $E_C := e^2/2C_\Sigma$. This is the energy needed to charge the island capacitance when adding one electron to the box. (Note the energy to add a Cooper pair is $(2e)^2/2C_\Sigma = 4E_C$.) With these definitions, our Hamiltonian becomes

$$\hat{H} = 4E_C(\hat{n} - n_g)^2 - E_J\cos\hat{\phi}. \tag{6.50}$$

Be careful that some references will define E_C as the charging energy of a Cooper pair instead of a single electron, and so the factor of 4 is dropped in front of E_C.

Charge Qubit Regimes

Equation (6.50) is the Hamiltonian for a general charge qubit. Different types of charge qubits are distinguished by their ratio E_J/E_C. The difference in this ratio will result in different system dynamics. For example, when $E_J/E_C \ll 1$, charging effects dominate tunnelling effects, with the implications that the number of Cooper pairs on the island is well defined and the energy of the system is very sensitive to the gate charge (or environmental charge). In the simplest circuit, with just a Josephson junction and gate capacitance, this ratio is controlled by varying the area, A, and critical current density, J_c, of the junction. (J_c is in turn controlled by the oxidation time and pressure used to form the tunnel barrier.) For a fixed J_c, $E_J \sim A$ and $E_C \sim 1/A$, implying $E_J/E_C \sim A^2$. For fixed A, $E_J/E_C \sim J_c$. (Since J_c depends exponentially on the thickness of the barrier, while C_J depends linearly, there is not a large change in C_J when we change J_c.) If we desire to further decouple E_J and E_C, we can increase the island capacitance by connecting a **shunt capacitor**, C_s, in parallel to our Josephson junction. The total capacitance of the island is then $C_\Sigma = C_s + C_J + C_g$.

We can start to understand the effect of E_J/E_C on the circuit dynamics by recalling that $\hat{n}$ and $\hat{\phi}$ are conjugate variables. This implies that if the uncertainty in one of these variables is small, the uncertainty in the other must be large. In the regime $E_J/E_C \ll 1$, often referred to as the charge regime, the number of the Cooper pairs on the island has a sharply peaked distribution, i.e. it is well defined. Conversely, the fluctuations of the phase are large. Because of this difference, the Cooper pair number basis is a good one in which to express the state of the system. (We sometimes then say that the Cooper-pair number is a good quantum number for the system.) In the context of charge qubits, the regime with $80 \gtrsim E_J/E_C \gg 1$ is often referred to as the transmon regime. In this regime, the qubit is less sensitive to charge noise, and Cooper pairs are not well localized on the island and, instead, ϕ becomes a good quantum number.

The CPB is a charge qubit in the regime of $E_J/E_C \ll 1$. Accordingly, it is useful to analyze the CPB starting in the **charge basis**, that is, using the eigenstates of $\hat{n}$,

$$\hat{n}\,|n\rangle = n\,|n\rangle\,. \tag{6.51}$$

Here, $|n\rangle$ represents the state with n excess Cooper pairs on the island, i.e. $n = 0$ would represent a charge-neutral island. Note that n can also be negative since Cooper pairs can be removed from the neutral state.

To express the Josephson term in the $|n\rangle$ basis, we first define the phase difference basis through the Fourier transform pair:

$$|\phi\rangle = \sum_{n=-\infty}^{\infty} e^{in\phi}|n\rangle, \qquad |n\rangle = \frac{1}{2\pi}\int_0^{2\pi} \mathrm{d}\phi e^{-in\phi}|\phi\rangle. \tag{6.52}$$

(We note that the discrete nature of n implies that ϕ is only well defined modulo 2π.) With these relations and the exponential operator,

$$e^{i\hat{\phi}} = \frac{1}{2\pi}\int_0^{2\pi} \mathrm{d}\phi e^{i\phi}\,|\phi\rangle\langle\phi|\,, \tag{6.53}$$

it is easy to show (see the exercises) that $e^{\pm i\hat{\phi}}|n\rangle = |n \mp 1\rangle$ or, equivalently,

$$e^{\pm i\hat{\phi}} \equiv \sum_{n=-\infty}^{\infty} |n \mp 1\rangle\langle n|\,. \tag{6.54}$$

The Josephson term can then be expressed as

$$E_J \cos\left(\hat{\phi}\right) = \frac{E_J}{2}(e^{i\hat{\phi}} + e^{-i\hat{\phi}}) \equiv \sum_{n=-\infty}^{\infty} \frac{E_J}{2}(|n\rangle\langle n+1| + |n+1\rangle\langle n|). \tag{6.55}$$

We see that the Josephson term explicitly takes the form of a tunnelling term when written in the charge basis. That is, it increases or decreases the number of Cooper pairs on the island by one when a tunnelling event occurs. Importantly, all the possible tunnelling events are summed coherently.

Using the language introduced in Section 2.6.5, we see that $\hat{\phi}$ is the generator of translations in $\hat{n}$. That said, we mention again that $\hat{n}$ and $\hat{\phi}$ are branch operators, and not necessarily canonical variables of our system, which is quantized in terms of node operators. Still, they are linear functions of the node operators, so we can still explicitly calculate their commutation relation based on the canonical commutation relations of the node operators.

It is easy to see that the charging (kinetic) part of the Hamiltonian is diagonal in the charge basis. We can thus write the total Hamiltonian of the charge qubit as

$$\hat{H} = \sum_{n=-\infty}^{\infty} 4E_C(n - n_g)^2\,|n\rangle\langle n| - \frac{E_J}{2}(|n\rangle\langle n+1| + |n+1\rangle\langle n|). \tag{6.56}$$

The charging term gives rise to a series of parabolas (one for each value of n) for the energy as a function of n_g (Fig. 6.10a). These parabolas intersect at half-integer values of n_g; these points are commonly referred to as the **charge degeneracy points**. However, the degeneracies disappear and we instead find a series of avoided crossings because of the Josephson term, which couples the different charging parabolas.

We can see this explicitly by analyzing the Hamiltonian near a degeneracy point, i.e. $n_g = 1/2$. In the CPB regime, we can restrict the analysis to only two states since $E_C \gg E_J$. These two states corresponding to $n = 0$ and $n = 1$ are denoted as $|0\rangle$ and $|1\rangle$. We have

$$\hat{H} = 4E_C\left(n_g - \frac{1}{2}\right)\hat{\sigma}_z - \frac{E_J}{2}\hat{\sigma}_x, \tag{6.57}$$

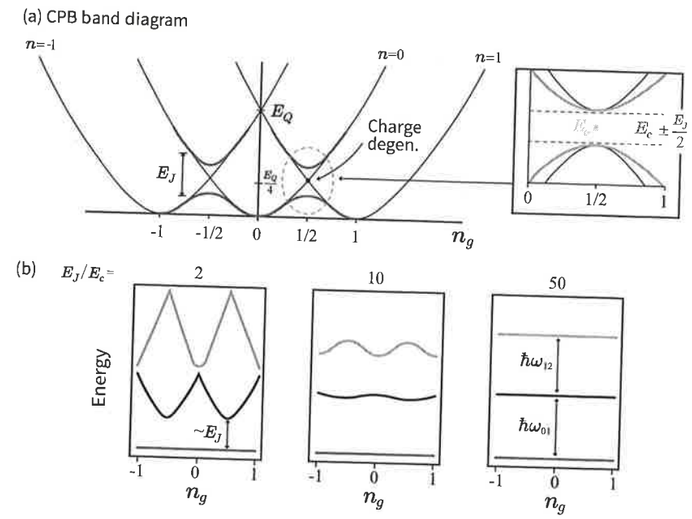

Fig. 6.10 **Different regimes for the charge qubit's energy band diagram.** (a) The energy band diagram for a CPB. (Inset) In the two-level approximation near $n_g = 1/2$, the energies are $E_{e/g} = \pm\frac{1}{2}\left(64E_C^2\left(n_g - \frac{1}{2}\right)^2 + E_J^2\right)^{1/2}$ shown in grey. (b) The energy diagrams for charge qubits with different E_J/E_C. As E_J/E_C increases into the transmon regime, the energy levels become less affected by variations in n_g and the system becomes more harmonic.

where we have dropped terms proportional to $\mathbb{1}$. This Hamiltonian also has eigenvalues $E_{e/g} = \pm\frac{1}{2}\left(64E_C^2\left(n_g - \frac{1}{2}\right)^2 + E_J^2\right)^{1/2}$. We can see from the eigenvalues that the energies are not degenerate at $n_g = \frac{1}{2}$, instead forming two hyperbolic bands with a minimum energy splitting of E_J. The next energy levels are separated by $\sim 4E_C$. Thus, for $E_C \gg E_J$, we have two well-isolated energy levels which we can use to encode a qubit.

6.3.2 Transmon

The CPB was the first superconducting circuit to successfully be used as a qubit. However, it became clear that environmental charge noise placed strong limits on the potential coherence times of the CPB. This led to the development of the so-called **transmon**. Historically, the transmon was viewed as a charge qubit in the regime of $E_J/E_C \sim 20$–80. As we will see below in detail, it can also naturally be viewed as an anharmonic oscillator. We can develop a qualitative appreciation for working in this regime by studying the transmon's spectrum. When studying a qubit's spectrum, what we measure are the transition frequencies between energy levels $\hbar\omega_{ij} = E_j - E_i$. The effect of different values of E_J/E_C on the transition frequencies between the ground state and the jth excited state as a function of n_g are shown in Fig. 6.10b. These plots were produced by numerically solving for the eigenvalues of the Hamiltonian in Eq. (6.50).

As we can see from Fig. 6.10b, there is one major advantage and one major disadvantage to increasing the value of E_J/E_C. The advantage is that the variation of the energy with respect to n_g decreases as E_J/E_C increases. This is crucial as environmental charge noise effectively leads to fluctuations in n_g and thus the qubit's transition frequency, leading to dephasing. The disadvantage is that, as E_J/E_C increases, the spectrum becomes more harmonic, which is something we want to avoid. If the anharmonicity decreases too much, the system simply stops being usable as a qubit, as the third and higher levels will be excited during qubit operations. More generally, limited anharmonicity implies limited control bandwidth and, thus, speed of gates.

Fortunately, there exists a sweet spot for the value of E_J/E_C to minimize the errors and maintain adequate nonlinearity, which is the transmon regime. This sweet spot exists because the anharmonicity decreases as $(E_J/E_C)^{-1/2}$ while the charge sensitivity decreases exponentially.

Complementary to the CPB, since $E_J \gg E_C$ for the transmon, it's better to analyze the transmon in the continuous $\hat{\phi}$ basis. Doing so, we can think of the dynamics of the system in analogy to a particle moving in a potential defined by the Josephson term of the Hamiltonian. For small oscillations around the equilibrium point $\langle\hat{\phi}\rangle = 0$, we can Taylor expand the Josephson energy and truncate it to fourth order, rewriting the Hamiltonian (Eq. (6.50)) as

$$\hat{H}_t = 4E_C\hat{n}^2 + \frac{E_J}{2}\hat{\phi}^2 - \frac{E_J}{24}\hat{\phi}^4, \tag{6.58}$$

where we have dropped the n_g term since its effects are small in the transmon regime and dropped a constant factor E_J.

The Hamiltonian Eq. (6.58) has the form of a harmonic oscillator with an anharmonic correction. Therefore, we will solve the Hamiltonian using perturbation theory, starting from the solution to the harmonic part. Accordingly, we introduce the following ladder operators:

$$\hat{\phi} = \phi_{\text{zpf}}(\hat{b}^\dagger + \hat{b}) \quad \text{and} \quad \hat{n} = in_{\text{zpf}}(\hat{b}^\dagger - \hat{b}), \tag{6.59}$$

where ϕ_{zpf} and n_{zpf} are the magnitudes of the zero-point fluctuations given by

$$\phi_{\text{zpf}} = \frac{1}{\sqrt{2}}\left(\frac{8E_C}{E_J}\right)^{1/4} \quad \text{and} \quad n_{\text{zpf}} = \frac{1}{\sqrt{2}}\left(\frac{E_J}{8E_C}\right)^{1/4}. \tag{6.60}$$

Here, we denote the transmon ladder operators as $\hat{b}^\dagger$ and $\hat{b}$ to distinguish them from ladder operators we'll encounter later. From the result that $[\hat{\phi}, \hat{n}] = i$, it follows that $[\hat{b}, \hat{b}^\dagger] = 1$,

$$1 = \frac{1}{i}\left[\hat{\phi}, \hat{n}\right] = \frac{1}{2}\left(\frac{8E_C}{E_J}\right)^{1/4}\left(\frac{E_J}{8E_C}\right)^{1/4}\left[\hat{b}^\dagger + \hat{b}, \hat{b}^\dagger - \hat{b}\right] = \left[\hat{b}, \hat{b}^\dagger\right]. \tag{6.61}$$

Using these ladder operators we can write our Hamiltonian as

$$\hat{H}_t = -E_C\left(\frac{E_J}{2E_C}\right)^{1/2}(\hat{b}^\dagger - \hat{b})^2 + \frac{E_J}{2}\left(\frac{2E_C}{E_J}\right)^{1/2}(\hat{b}^\dagger + \hat{b})^2 - \frac{E_J}{24}\left(\frac{2E_C}{E_J}\right)(\hat{b}^\dagger + \hat{b})^4 \tag{6.62}$$

$$= \sqrt{8E_JE_C}\left(\hat{b}^\dagger\hat{b} + \frac{1}{2}\right) - \frac{E_C}{12}(\hat{b}^\dagger + \hat{b})^4. \tag{6.63}$$

Written in this way, the transmon's resemblance to a harmonic oscillator with a small anharmonic deviation is clear. The harmonic resonance frequency of the oscillator is $\hbar\omega_0 = \sqrt{8E_JE_C}$. The prefactor of the nonlinear term is $\frac{E_C}{12}$, which is small compared to $\hbar\omega_0$ when

$$\sqrt{8E_JE_C} \gg \frac{E_C}{12} \quad \Rightarrow \quad \frac{E_J}{E_C} \gg \frac{1}{(12^2)(8)} \approx 9 \times 10^{-4}. \tag{6.64}$$

This clearly holds in the transmon regime of $E_J/E_C \sim 20$–80. We will also drop terms with an unequal number of raising and lowering operators. In the interaction picture of the unperturbed harmonic oscillator Hamiltonian, the creation operator acquires a time dependence $e^{i\omega_q t}\hat{b}^\dagger$ where ω_q is the oscillator frequency. Therefore, any terms with an unequal number of creation and annihilation operators will have a time-dependent phase, such as $e^{\pm 2i\omega_q t}$. We can apply a rotating-wave approximation to drop these terms so long as $\hbar\omega_q \gg E_C/4$, which is true in the transmon regime. Thus, we find the transmon Hamiltonian to be

$$\hat{H}_t = \hbar\omega_q\left(\hat{b}^\dagger\hat{b} + \frac{1}{2}\right) + \frac{\hbar\alpha}{2}\hat{b}^\dagger\hat{b}^\dagger\hat{b}\hat{b}, \tag{6.65}$$

where we have dropped a constant term of $-\frac{E_C}{4}$ that appears and introduced the **anharmonicity** $\alpha := \omega_{12} - \omega_{01}$, where $\omega_{ij} = (E_j - E_i)/\hbar$ is the transition frequency (see exercises). We have also defined the qubit frequency as $\omega_q := \omega_{01} = \sqrt{8E_CE_J} - E_C$ (which includes the first-order energy shift, E_C), since we encode the qubit in the ground state and the first excited state, $|g\rangle$ and $|e\rangle$.

The anharmonicity of the transmon is a key parameter. First, we require $\alpha \gg \Gamma_2, \Gamma_1$ ($\Gamma_1 = 1/T_1, \Gamma_2 = 1/T_2$). Otherwise, the circuit will not behave as a qubit. Second, α limits how fast the transmon can be controlled. Roughly, the minimum gate time is $\approx 1/\alpha$. If this speed limit is violated, the spectrum of a control pulse centered at ω_{01} will still have significant power at ω_{12}. (See the discussion of hard and soft control pulses in Chapter 3.) The anharmonicity of a transmon is typically designed to be in the range $\alpha/2\pi \approx 100$–400 MHz. With this range for α, we can maintain a large ratio of E_J/E_C with a qubit frequency of $\omega_q/2\pi \approx 4$–8 GHz. Since $|\alpha| \ll \omega_q$, we have that the transmon is essentially an anharmonic oscillator. As we'll find in the exercises, $\alpha = -\frac{E_C}{\hbar} = -\frac{e^2}{2\hbar C_\Sigma}$. This relation makes it clear that there is a design trade-off between the anharmonicity, which controls the gate speed, and the sensitivity to charge noise, which grows with E_C.

At different points of this chapter we will simplify our Hamiltonian by making the **two-level approximation**, in which we restrict ourselves to the two-qubit levels of the transmon. We can justify such an approximation by suppressing excitations to higher noncomputational states. We can achieve this suppression by making $|\alpha|$ larger or by using pulse-shaping techniques as we introduced in NMR. In this two-level approximation, the raising operator's only function is to map the ground state to the excited state, $\hat{b}^\dagger = |e\rangle\langle g| \equiv \hat{\sigma}_+$ and the lower operators is to map the excited state to the ground state $\hat{b} = |g\rangle\langle e| \equiv \hat{\sigma}_-$. As a result we also find that $\hat{b}^\dagger\hat{b} = |e\rangle\langle e|$, $\hat{b}\hat{b}^\dagger = |g\rangle\langle g|$, $\hat{b}^\dagger\hat{b}^\dagger\hat{b}\hat{b} = 0$. For consistency with the other chapters, we encode the logical 0 in the ground state and the logical 1 in the excited

state. Thus, $-\hat{\sigma}_z = \hat{b}^\dagger\hat{b} - \hat{b}\hat{b}^\dagger = 2\hat{b}^\dagger\hat{b} - \hat{\mathbb{1}}$. The transmon Hamiltonian under the two-level approximation reduces to

$$\hat{H}_t = -\frac{\hbar\omega_q}{2}\hat{\sigma}_z. \tag{6.66}$$

This approximation assumes that $b^\dagger|e\rangle = 0$, which makes sense if we have high anharmonicity. Still, we should keep in mind that higher energy levels do exist. We will later use these higher energy levels for qubit control and measurement, similar to what we did with trapped ions.

6.3.3 Tunable Transmon

An important variant of the transmon is the **tunable transmon**, also known as the **split transmon**. Building a tunable transmon involves replacing the Josephson junction in the transmon with a DC-SQUID. Thus, its Hamiltonian is

$$\hat{H}_{\text{st}} = 4E_C\hat{n}^2 - E_{J1}\cos\hat{\phi}_1 - E_{J2}\cos\hat{\phi}_2, \tag{6.67}$$

where E_{Ji} and $\hat{\phi}_i$ are, respectively, the Josephson energy and the phase difference across the ith Josephson junctions. In the presence of an external flux Φ_{ext}, flux quantization requires that $\hat{\phi}_1 - \hat{\phi}_2 + \frac{2\pi}{\Phi_0}\Phi_{\text{ext}} = 0\text{mod}(2\pi)$. By defining $\phi_{\text{ext}} \coloneqq \frac{\pi}{\Phi_0}\Phi_{\text{ext}}$ and the average phase difference $\hat{\phi}_{\text{avg}} \coloneqq (\hat{\phi}_1 + \hat{\phi}_2)/2$, we can rewrite Eq. (6.67) as

$$\hat{H}_{\text{st}} = 4E_C\hat{n}^2 - E_J(\phi_{\text{ext}})\cos\left(\hat{\phi}_{\text{avg}} - \phi_0\right), \tag{6.68}$$

where

$$E_J(\phi_{\text{ext}}) = E_{J\Sigma}\sqrt{\cos^2(\phi_{\text{ext}}) + d^2\sin^2(\phi_{\text{ext}})}\,, \tag{6.69}$$

$E_{J\Sigma} \coloneqq E_{J1} + E_{J2}$, $d \coloneqq (E_{J2} - E_{J1})/E_{J\Sigma}$, and $\phi_0 \coloneqq d\tan(\phi_{\text{ext}})$. By adjusting an external flux, Φ_{ext}, applied to the transmon, we can tune ϕ_{ext}, adjust its effective E_J and thus its qubit frequency ω_q.

6.3.4 Other Superconducting Qubits

As of writing this text, the transmon is the most developed of the superconducting qubits. It is the one most used. While the transmon is the focus of this chapter, we'll briefly survey some of the other superconducting qubits here.

The simplest flux qubit is the RF-SQUID qubit, which, in many ways, can be thought of as the electromagnetic dual of the CPB. An RF-SQUID qubit (depicted in Fig. 6.11a) is made from a superconducting loop with inductance L interrupted by a single Josephson junction. Complementary to the charge bias gate capacitively coupled to the CPB island, the flux qubit is biased by an external magnetic flux inductively coupled to the flux qubit loop.

Comparing the circuit in Fig. 6.11a to the CPB, the inductor has replaced the capacitor and a magnetic flux bias has replaced the voltage bias. For the CPB, the applied voltage controls the tunnelling of Cooper pairs on or off of the CPB's island. Here, the applied flux controls the tunnelling of magnetic flux quanta in to or out of the loop.

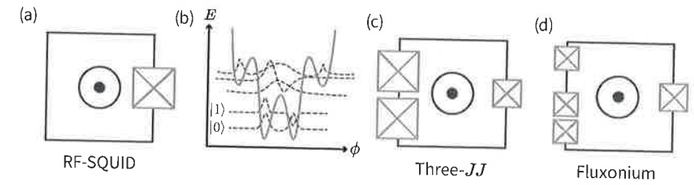

Fig. 6.11 **Flux qubits.** (a) The circuit diagram for the RF-SQUID flux qubit. The qubit loop is penetrated by an external magnetic flux that controls the flux bias, ϕ_{ext}. (b) The potential for the RF-SQUID flux qubit. The two lowest energy level states are used to encode the qubit. (c) The three-junction flux qubit, which essentially replaces the magnetic inductance of the RF-SQUID with the Josephson inductance of the additional junctions. Qualitatively, its potential landscape is very similar to (b). (d) The fluxonium is a more recent qubit that replaces the two large junctions of the flux qubit with an array of many junctions. While still controlled by a flux bias, the dynamics are substantially different from the other flux qubits.

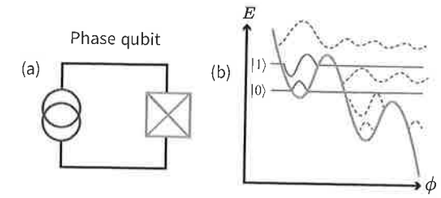

Fig. 6.12 **Phase qubit.** (a) The circuit diagram for the phase qubit, showing a large Josephson junction biased by a current source. (b) The potential for the phase qubit. The junction is biased until only a few states remain in the metastable well. The lowest two states are used as the qubit states.

Dual to the CPB, it is convenient to describe the flux qubit in the phase basis. With an external flux bias near one half of a flux quantum, the low-energy part of the flux qubit potential forms a double-well potential. Roughly, the two states of the qubit, one in each well, represent a persistent current circulating in the loop either clockwise or counterclockwise. Alternatively, this can be thought of as a small magnetic moment pointing up or down, not unlike a spin. Because of quantum tunnelling between the wells, however, these two states hybridize, with the final qubit states being the even and odd superposition of the clockwise and counter-clockwise states.

The most notable variation of the flux qubit is the **three-junction flux qubit**, which is often referred to as *the* flux qubit (see Fig. 6.11c). The relatively large inductance value required to make the RF-SQUID flux qubit requires having a physically large inductor coil, which unfortunately also serves as a good antenna for electromagnetic interference. The three-junction flux qubit removes the large, geometric inductor and replaces it with additional Josephson junctions, using their Josephson inductance in place of the geometric inductance.

Another historical qubit archetype is the **phase qubit**. The phase qubit is essentially a large, current-biased Josephson junction (Fig. 6.12a). The phase qubits have an E_J/E_C ratio which is many orders of magnitude larger than the other qubits we've studied, $\sim 10^6$.

Its potential energy has a washboard shape, as seen in Fig. 6.12b. When properly current biased, one well of the washboard potential will host only a few quantum states. The two qubit levels of the phase qubit are then the two lowest energy levels in the well. Other auxiliary levels can be used, e.g. for readout. Phase qubits were one of the early superconducting qubits, producing many important results. However, like the CPB, they are rarely used now because they suffered from low coherence times related to defects in the large-area tunnel barriers.

A relatively recent addition to the superconducting qubit zoo is the so-called **fluxonium**. The fluxonium takes the basic idea of the three-junction flux qubit much further, adding a long array of junctions (see Fig. 6.11d). While still controlled by a flux bias, the dynamics and energy-level diagram are substantially different from the other flux qubits. Despite the relative complexity of the array of junctions, fluxonium has demonstrated coherence times approaching those of transmons. It also offers some potential advantages, such as the ability to operate at lower frequencies than transmons, where the cost and complexity of control electronics is potentially lower.

6.4 Circuit Quantum Electrodynamics

We will now introduce an important paradigm within superconducting quantum circuits, known as **circuit quantum electrodynamics** (QED). At a fundamental level, circuit QED is the study of the interaction between superconducting qubits and quantized electromagnetic fields inside a resonator. At a practical level, circuit QED has played a major role in the development of quantum computing with superconducting circuits. Among other things, it allowed for stronger coupling between the qubits and photons, for mitigating the effects of decoherence, and has led to new ways of performing two-qubit gates and measurements.

Throughout this section, we'll build up to the central Hamiltonian of circuit QED, the one which describes the interaction between a superconducting qubit and a resonator. We'll first use circuit QED's predecessor, cavity QED, as a springboard into the topic (Section 6.4.1). It provides a simpler setting to introduce the underlying physics of the interaction. In Section 6.4.2, we'll study a waveguide resonator's structure and Hamiltonian. Using these Hamiltonians, we'll then find that the interaction between the qubits and the resonator takes the form of the well-studied Jaynes–Cummings Hamiltonian, which we study in Section 6.4.3. This Hamiltonian can take different forms depending on the detuning between the qubit and the resonator. Finally, we'll conclude in Section 6.4.4 by exploring a particular detuning useful for quantum computing, the so-called dispersive regime.

6.4.1 Cavity QED

Circuit QED was inspired by and closely resembles **cavity QED**. In cavity QED, we place atoms inside an electromagnetic **cavity** formed by two mirrors. We then study the quantum interaction between the atom and the quantized electromagnetic field in the cavity. The cavities can operate at optical or microwave frequencies, interacting with the corresponding

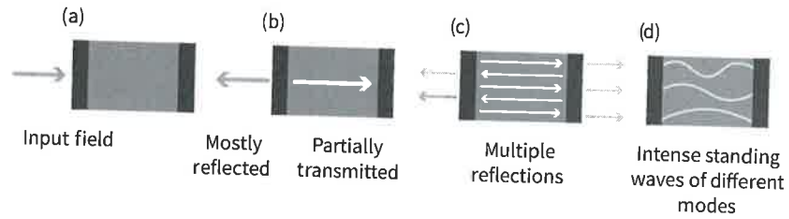

Fig. 6.13 **Working principle of a Fabry–Pérot cavity.** (a) An input field is incident on the cavity. (b) The field is mostly reflected, and a small portion is transmitted. (c) The field reflects multiple times inside the cavity. (d) The multiple reflections lead to constructive and destructive interference, leaving only discrete modes with a stable field configuration. The existence of these discrete modes leads to a series of peaks when we measure the transmission of the cavity as a function of frequency, as shown in Fig. 6.14.

transitions in the atom. Cavity QED provides a way to study the interaction between single atoms and single photons. Until this point in the text, when studying the interaction between light and qubits, we treated the interaction semiclassically, i.e. ignoring the light's quantum nature. In this section, we'll no longer do this.

The primary purpose of the cavity in cavity QED is to increase the coupling strength between the atom and photons in the cavity. Colloquially, the cavity allows a single photon to interact with the atom multiple times as the photon bounces back and forth between the mirrors that form the cavity. In this way, cavity QED allows us to observe the interaction of a single photon with a single atom. At the same time, the cavity causes the spectrum of the electromagnetic field inside to become discrete, in contrast to the continuous spectrum of free space. It also helps in isolating the atom from the noise of the environment.

How an optical cavity discretizes the electromagnetic field can be understood by studying a simple electromagnetic cavity, the **Fabry–Pérot cavity**. It consists of two mirrors facing one another. One or both mirrors will be made slightly transparent so that a small fraction of light incident on the mirror can enter or leave the cavity, as shown in Fig. 6.13. Once inside the cavity, the light will reflect between the two mirrors many times before leaking out. These multiple reflections interfere with each other, and only a discrete set of frequencies will interfere constructively. These frequencies correspond to wavelengths $\lambda_n = 2l/n$, where l is the length of the cavity and n is a positive integer. These wavelengths correspond to the resonant modes of the cavity (Fig. 6.13d). The resonant frequencies can be experimentally determined by measuring the intensity of light transmitted through the cavity (assuming it has two slightly leaky mirrors). Similar to what is depicted in Fig. 6.14 for a waveguide cavity, the transmission measured as a function of frequency shows a series of peaks corresponding to the resonant frequencies.

In both circuit and cavity QED, we often work in the **single-mode approximation**. In this approximation, we focus on the coupling between the atom and just a single mode of the cavity. Within this approximation, we then treat the mode of interest as a quantum harmonic oscillator. To work in this approximation, we set the bandwidth of the input field to be in the range of only one of the cavity's modes, selecting that single mode.

At a conceptual level, circuit QED is essentially identical to cavity QED. Experimentally, in circuit QED we use an artificial atom (a superconducting qubit) instead of a natural atom and an on-chip microwave waveguide resonator in place of a 3D cavity.

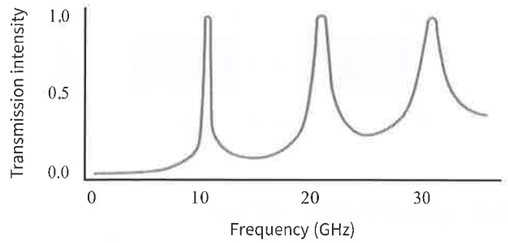

Fig. 6.14 **Cavity transmission intensity.** The transmission peaks as a function of the frequency. In this figure, the line widths increase for subsequent peaks. What's depicted here is the steady-state behaviour of the cavity. Figure 6.13 describes how the cavity reaches the steady state.

6.4.2 Waveguide Resonators

To move from cavity QED to circuit QED, we replace the 3D cavity by a microfabricated waveguide resonator typically operating in the microwave regime. A **waveguide** is a structure that confines and guides electromagnetic waves. In circuit QED they are typically made by patterning superconducting films on dielectric substrates. By adding boundary conditions at two ends of our waveguide, we turn it into a **waveguide resonator**. In cavities, the mirrors impose a boundary condition on the electromagnetic field, specifically that the electric field is zero at the surface of the mirrors. The waveguide resonators operate in a similar way, imposing either an open-circuit (zero current) or short-circuit (zero voltage) boundary condition at the ends of the resonator. The resonators are typically designed in the microwave regime consistent with the qubit frequencies.

There exist different types of on-chip waveguides. The most common is the **coplanar waveguide**, which is illustrated in Fig. 6.15a. It consists of a center conductor with a spatial gap on each side of it separating it from the ground-plane conductors. One can imagine a slice of the coaxial cable bringing TV signals into your house. Like the cable, the waveguide tightly confines the microwaves in the two transverse dimensions while allowing them to propagate along the third dimension. Typical superconducting metals are aluminum or niobium. Typically substrate materials are sapphire or undoped silicon.

We can consider a resonator with two open-circuit boundary conditions, like the one depicted in Fig. 6.15a. It is known as a $\lambda/2$ resonator, having resonant wavelengths defined by $\lambda_m = 2d/(m+1)$, where m is a nonnegative integer and d is the length of the resonator. For each wavelength, there will be a corresponding frequency. The spectrum of the resonator is illustrated in Fig. 6.14. The lowest resonance frequency, often called the fundamental frequency and corresponding to λ_0, is given by $f_0 = v/2d$ with all resonance frequencies given by $f_m = (m+1)f_0$. Here, $v = 1/\sqrt{l_0 c_0}$ is the speed of light in the waveguide, c_0 is the capacitance per unit length, and l_0 is the inductance per unit length of the waveguide. Both c_0 and l_0 are design parameters, but typically $v \sim 1 \times 10^8$ m/s, about one-third of the speed of light in a vacuum.

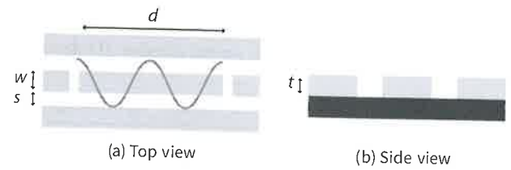

Fig. 6.15 **2D coplanar waveguide resonator.** It consists of a central conductor with a spatial gap on each side separating it from ground-plane conductors. The outer ground planes extend much farther than are shown in the diagram and are ideally semi-infinite. Note that the drawing is not to scale. The waveguides are made from thin metal films (~100 nm), forming an approximately two-dimensional structure. The coplanar waveguide can operate as a resonator by imposing boundary conditions on the central conductor. These boundary conditions can be imposed by either patterning open gaps in the central conductor, which result in open-circuit (zero current) boundary conditions, or by connecting the central conductor to the ground planes, resulting in short-circuit (zero voltage) boundary conditions. The open-circuit boundary condition is illustrated in the figure.

As with the 3D cavity modes above, we can apply the single-mode approximation to describe the coplanar waveguide resonator as a **lumped-element LC oscillator**. We refer to devices as "lumped-element" when we can ignore the spatial extent of their modes. The particular values of the lumped-element inductance, L_r, and capacitance, C_r, can be derived in different ways, e.g. as the weighted average of l_0 and c_0 over the spatial-mode structure. This implies that the values of L_r and C_r are functions of the mode number, m. The Hamiltonian of a single mode of the cavity can be written in the standard way as

$$\hat{H}_r = \hbar\omega_r \left(\hat{a}^\dagger \hat{a} + \frac{1}{2}\right), \tag{6.70}$$

where $\hat{a}^\dagger$ denotes the creation operator of the resonator mode and ω_r its angular frequency.

To add the artificial atom to our system, we typically capacitively couple a transmon to the waveguide resonator. In early designs, the transmon was placed inside the gap between the center conductor and the ground plane of the waveguide resonator. While the network of physical capacitance can be complex, standard circuit techniques allow us to represent the coupling by a single "coupling" capacitance, C_c.

While 2D waveguides will be the focus of this chapter, we can also consider using 3D resonators in the microwave regime. Each dimension of these resonators is made to be on the order of centimetres to produce resonance frequencies in the microwave range. Historically, so-called 3D transmon architectures made an important contribution to understanding decoherence in superconducting qubits and resonators. The lesson was that much of the decoherence at the time came from material defects on the surfaces and interfaces of the metals and substrate used to make the qubit. Using a 3D resonator, less of the field energy is stored at the surface and interfaces, so less loss occurs. The lessons learned from 3D transmons were successfully translated back into two-dimensional architectures, such as transmon arrays, which continue to dominate. Still, 3D architectures are used for some

alternative approaches where the qubits are encoded in the cavity modes. For pedagogical purposes, it's sufficient to focus on the simpler 2D design.

6.4.3 Jaynes–Cummings Model

Equipped with the Hamiltonian of the transmon and the waveguide resonator, we can now study their interaction, which is given by the **Jaynes–Cummings Hamiltonian**. This is a well-studied Hamiltonian that represents the exchange of a single photon between a harmonic oscillator and a two-level system.

To derive the Jaynes–Cummings Hamiltonian, we consider a transmon and waveguide resonator that are capacitively coupled. Since the resonator is an extended object, the full treatment is somewhat complex, but we can reduce the problem to that of a lumped-element LC resonator coupled to the transmon through a capacitance C_c (Fig. 6.16).

We can now derive the full Hamiltonian for the transmon, resonator, and coupling interaction. To do so, we need to determine the new terms to be added to the Lagrangian of the circuit and then derive the Hamiltonian using the Legendre transformation. First, consider how C_c would add to the circuit's Lagrangian. Φ_r and Φ_t are the resonator and transmon flux. Recall that $\dot{\Phi}_r$ and $\dot{\Phi}_t$ are the voltages across the resonator and transmon, and then $(\dot{\Phi}_r - \dot{\Phi}_t)$ is the voltage across C_c. The energy contributed by C_c is

$$\mathcal{T}_{\text{int}} = \frac{C_c}{2}\left(\dot{\Phi}_r - \dot{\Phi}_t\right)^2. \tag{6.71}$$

The terms that are proportional to $\dot{\Phi}_r^2$ and $\dot{\Phi}_t^2$ will just add to the capacitive energies of the transmon and resonator, producing static frequency shifts. The cross term $C_c\dot{\Phi}_r\dot{\Phi}_t/2$ is then the interaction energy resulting from the coupling. To find the exact expression for the Hamiltonian with Eq. (6.71) included in the Lagrangian requires using the Legendre transformation. We don't include this calculation here, but give the expression for the new term after assuming that $C_c \ll C_r, C_\Sigma$. When we transform to the Hamiltonian and quantize the circuit, this leads to the interaction Hamiltonian

$$\hat{H}_{\text{int}} = \frac{C_c}{C_r C_\Sigma}\hat{Q}_t\hat{Q}_r = -\hbar g(\hat{b}^\dagger - \hat{b})(\hat{a}^\dagger - \hat{a}), \tag{6.72}$$

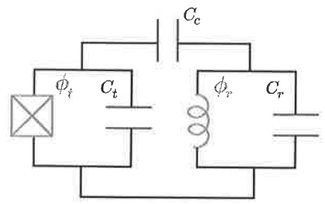

Fig. 6.16 **Transmon capactively coupled to a waveguide resonator.** Here we model one mode of the resonator as a lumped-element LC resonator. The capacitance of the transmon $C_\Sigma = C_t + C_J$ includes a component from the capacitance of the transmon's Josephson junction C_J.

where g is known as the **oscillator–transmon coupling constant** or the **light–matter coupling constant**,

$$g = \omega_r\sqrt{\frac{Z_r e^2}{2\hbar}}\frac{C_c}{C_\Sigma}\left(\frac{E_J}{2E_C}\right)^{1/4}. \tag{6.73}$$

Thus, the full Hamiltonian for the system consists of the Hamiltonians of the resonator, Eq. (6.70), the transmon (before the two-level approximation), Eq. (6.65), and the capacitive coupling interaction. Together we have

$$\begin{aligned}\hat{H} &= \hat{H}_r + \hat{H}_t + \hat{H}_{\text{int}},\\ &= \hbar\omega_r\hat{a}^\dagger\hat{a} + \hbar\omega_q\left(\hat{b}^\dagger\hat{b} + \frac{1}{2}\right) - \frac{E_C}{2}\hat{b}^\dagger\hat{b}^\dagger\hat{b}\hat{b} - \hbar g(\hat{b}^\dagger - \hat{b})(\hat{a}^\dagger - \hat{a}).\end{aligned} \tag{6.74}$$

We can now simplify the Hamiltonian in two steps. The first step is to apply a rotating-wave approximation. In the rotating frame of the uncoupled Hamiltonian $\hat{H}_0 = \hbar\omega_r\hat{a}^\dagger\hat{a} + \hbar\omega_q(\hat{b}^\dagger\hat{b} + \frac{1}{2})$ the $\hat{a}$ ($\hat{a}^\dagger$) operator evolves as $\hat{a}e^{-i\omega_r t}$ ($\hat{a}^\dagger e^{i\omega_r t}$) and the $\hat{b}$ ($\hat{b}^\dagger$) operator evolves as $\hat{b}e^{-i\omega_q t}$ ($\hat{b}^\dagger e^{i\omega_q t}$). Thus, in this rotating frame, the interaction term has the form

$$\hat{H}_{\text{int}}^{(I)} = \hbar g\left(\hat{b}^\dagger\hat{a}^\dagger e^{i(\omega_q+\omega_r)t} + \hat{b}^\dagger\hat{a}e^{i(\omega_q-\omega_r)t} + \hat{b}\hat{a}^\dagger e^{i(-\omega_q+\omega_r)t} + \hat{b}\hat{a}e^{i(-\omega_q-\omega_r)t}\right). \tag{6.75}$$

Assuming we are near resonance, i.e. $|\omega_q - \omega_r| \ll |\omega_q + \omega_r|$, we drop the quickly oscillating terms. Transforming back to the lab frame, we find

$$\hat{H} = \hbar\omega_r\hat{a}^\dagger\hat{a} + \hbar\omega_q\left(\hat{b}^\dagger\hat{b} + \frac{1}{2}\right) - \frac{E_C}{2}\hat{b}^\dagger\hat{b}^\dagger\hat{b}\hat{b} + \hbar g(\hat{b}^\dagger\hat{a} + \hat{b}\hat{a}^\dagger). \tag{6.76}$$

The next step is to apply the two-level approximation for the transmon and find

$$\hat{H}_{\text{JC}} \coloneqq \hbar\omega_r\hat{a}^\dagger\hat{a} - \frac{\hbar\omega_q}{2}\hat{\sigma}_z + \hbar g(\hat{\sigma}_+\hat{a} + \hat{\sigma}_-\hat{a}^\dagger). \tag{6.77}$$

This is the Jaynes–Cummings Hamiltonian, $\hat{H}_{\text{JC}}$. This is a well-studied Hamiltonian that is exactly solvable. The last term corresponds to our transmon and resonator interacting through a coherent exchange of a photon in the resonator and of an excitation of the transmon. Some texts will flip the sign of the $\frac{\hbar\omega_q}{2}\hat{\sigma}_z$ term in the Jaynes–Cummings Hamiltonian. We choose the sign convention that is consistent with the rest of this text.

We now turn to finding the eigenstates and eigenvalues of the Jaynes–Cummings Hamiltonian. We start by writing $\hat{H}_{\text{JC}}$ in the basis of the **bare states**. The bare states are the joint eigenstates of the qubit and the resonator when there is no coupling term. These states take the form of $|g/e\rangle \otimes |n\rangle$, where n is the photon number of the resonator.

We can introduce the operator $\hat{N}_{tr}$ that counts the total number of excitations in the bare states, $\hat{N}_{tr} = \hat{\sigma}_+\hat{\sigma}_- + \hat{a}^\dagger\hat{a}$. In doing so, we find that it has two pertinent properties. The first is that, since the pairs of states $|e, n-1\rangle$ and $|g, n\rangle$ have an equal number of excitations, the eigenvalues of the operator $\hat{N}_{tr}$ are degenerate. Second, $\hat{N}_{tr}$ commutes with $\hat{H}_r$ and $\hat{H}_t$ and with the full $\hat{H}_{\text{JC}}$,

$$\left[\hat{H}_{\text{JC}}, \hat{N}_{tr}\right] = \left[\hat{H}_{\text{int}}, \hat{N}_{tr}\right] = \hbar g\left[\hat{a}\hat{\sigma}_+ + \hat{a}^\dagger\hat{\sigma}_-, \hat{a}^\dagger\hat{a} + \hat{\sigma}_+\hat{\sigma}_-\right] = 0, \tag{6.78}$$

and therefore the total number of excitations is conserved by $\hat{H}_{\text{JC}}$.

Because of these two properties, we can write $\hat{H}_{\text{JC}}$ as a block-diagonal matrix in the basis of the bare states ordered as, $\{|g,0\rangle, |e,0\rangle, |g,1\rangle, |e,1\rangle, |g,2\rangle, \ldots\}$. The diagonal blocks will occur in each of the degenerate 2×2 subspaces of $\{|e,n-1\rangle, |g,n\rangle\}$, except for the $n = 0$ case in which there's only one state, $|g,0\rangle$. Thus, we have the matrix:

$$\hat{H}_{\text{JC}} = \begin{bmatrix} \hat{H}_{\text{JC}}^{(0)} & & & \\ & \hat{H}_{\text{JC}}^{(1)} & & \\ & & \hat{H}_{\text{JC}}^{(2)} & \\ & & & \ddots \end{bmatrix}. \tag{6.79}$$

Each block-diagonal component ($n \geq 1$) can be written as

$$\begin{aligned} \hat{H}_{\text{JC}}^{(n)} &= \begin{bmatrix} \langle e,n-1|\hat{H}_{\text{JC}}|e,n-1\rangle & \langle e,n-1|\hat{H}_{\text{JC}}|g,n\rangle \\ \langle g,n|\hat{H}_{\text{JC}}|e,n-1\rangle & \langle g,n|\hat{H}_{\text{JC}}|g,n\rangle \end{bmatrix} \\ &= \hbar \begin{bmatrix} (n-1)\omega_r + \frac{\omega_q}{2} & g\sqrt{n} \\ g\sqrt{n} & n\omega_r - \frac{\omega_q}{2} \end{bmatrix} \\ &= \hbar\omega_r(n - \frac{1}{2})\hat{\mathbb{1}} + \frac{\hbar\Delta}{2}\hat{\sigma}_z + \hbar g\sqrt{n}\hat{\sigma}_x, \end{aligned} \tag{6.80}$$

where $\Delta := \omega_q - \omega_r$ is the detuning between the qubit and the resonator. Note that in this latter equation, the Pauli matrices $\hat{\sigma}_z$ and $\hat{\sigma}_x$ belong to the Hilbert space of the states $|g,n\rangle$ and $|e,n-1\rangle$. To be clear, this $\hat{\sigma}_z$ is not in the qubit basis. The block Hamiltonian $\hat{H}_{\text{JC}}^{(n)}$ has the form of a coupled two-state system. We also note that each subspace of states $|g,n\rangle$ and $|e,n-1\rangle$ is decoupled from all other states.

Finding the eigenvalues and eigenstates of $\hat{H}_{\text{JC}}$ is now straightforward given its decomposition into diagonal blocks that are sums of Pauli matrices. Using Eq. (2.161), we find that that $\hat{H}_{\text{JC}}^{(n)}$ has eigenvalues,

$$E_{\pm,n} = \hbar\omega_r(n - \frac{1}{2}) \pm \hbar\sqrt{g^2 n + \frac{\Delta^2}{4}}, \tag{6.81}$$

and eigenstates,

$$|+,n\rangle = \cos\left(\frac{\theta_n}{2}\right)|e,n-1\rangle + \sin\left(\frac{\theta_n}{2}\right)|g,n\rangle, \tag{6.82}$$

$$|-,n\rangle = -\sin\left(\frac{\theta_n}{2}\right)|e,n-1\rangle + \cos\left(\frac{\theta_n}{2}\right)|g,n\rangle, \tag{6.83}$$

where $\theta_n = \arctan(2g\sqrt{n}/\Delta)$. The states $|\pm,n\rangle$ are known as the **dressed states**, with the idea that the bare matter (qubit) states are "dressed" by the photons. The dressed ground state equals the ground state, $|-,0\rangle := |g,0\rangle$, and it has an energy $-\hbar\frac{\omega_q}{2}$.

6.4.4 Detuning Regimes

The Jaynes–Cummings Hamiltonian (Eq. (6.80)) has two different behaviours depending on the value of Δ: the on-resonance and dispersive regimes.

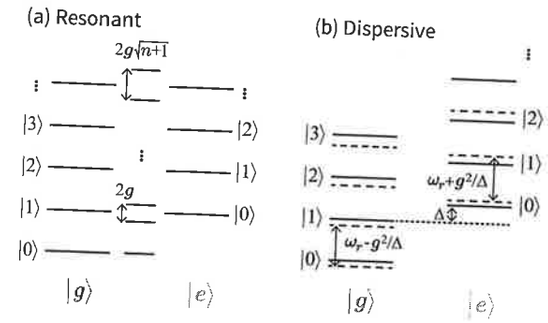

Fig. 6.17 **Jaynes–Cummings Hamiltonian's spectrum.** The spectrum for the (a) resonant regime, $\Delta = 0$, and (b) the dispersive regime $|\Delta/g| \gg 1$. In panel (a), the outer lines show the uncoupled energies, while the central lines show the dressed energies. In panel (b), the solid lines show the uncoupled energy levels, while the dotted lines show dressed energies. This figure is adapted from Blais et al. (2004).

In the on-resonance regime, the frequency of the transmon and the resonator are equal, $\omega_r = \omega_q$ and $\Delta = 0$. In that case, $\theta_n = \pi/2$ and Eqs. (6.82) and (6.83) reduce to the **resonant eigenstates**,

$$|+,n\rangle = \frac{1}{\sqrt{2}}(|g,n\rangle + |e,n-1\rangle), \tag{6.84}$$

$$|-,n\rangle = \frac{1}{\sqrt{2}}(|g,n\rangle - |e,n-1\rangle). \tag{6.85}$$

Their spectrum and the spectrum of the bare states are given in Fig. 6.17a. For the resonant eigenstates, the states of the transmon and the resonator are maximally entangled, which complicates encoding the qubit in the resonant eigenstates. Furthermore, in the resonant regime the cavity will greatly enhance the relaxation rate of the qubit; this is known as the Purcell effect (which we discuss in Section 6.8).

In this regime, it's easy to observe an interesting quantum effect known as **vacuum Rabi oscillations**. Consider placing an excited qubit in a resonator in the vacuum state, giving the initial state $|e,0\rangle$. We know from the Jaynes–Cummings Hamiltonian that this state will couple to $|g,1\rangle$, causing periodic oscillations between the two. These are known as vacuum Rabi oscillations.

Even though the on-resonance regime isn't typically used directly in quantum computing, it's an important model of light–matter interaction and is seen in various other applications of circuit QED.

One common regime we work in is the **dispersive regime**, where the detuning between the transmon and resonator is large with respect to the coupling between them, $|\Delta|/|g| \gg 1$. As a result, in this regime the qubit and resonator energy eigenstates are only weakly entangled. Different protocols for measurements and two-qubit gates become possible in this regime. The large difference in frequency makes it such that the transmon and the resonator cannot exchange excitations directly.

We now look to find solutions to the Jaynes–Cummings model in the dispersive regime. In the two-level approximation, Eqs. (6.81)–(6.83) are exact, and we can find expressions

for the energies and states by expanding them for $|\Delta|/|g| \gg 1$. At the same time, it is instructive to find an approximate form of the Hamiltonian in the dispersive regime, which can be done in different ways. One approach, valid in the two-level approximation, is to apply the dispersive transformation

$$\hat{U} = \exp\left[\frac{g}{\Delta}(\hat{\sigma}_+\hat{a} - \hat{\sigma}_-\hat{a}^\dagger)\right]. \tag{6.86}$$

We'll explore this approach in detail in the exercises, but for now we just write the result. We find that the transmon Hamiltonian in the dispersive regime is

$$\hat{H}_{\text{disp}} = \hbar\omega_r'\hat{a}^\dagger\hat{a} - \frac{\hbar\omega_q'}{2}\hat{\sigma}_z - \hbar\chi\hat{\sigma}_z\hat{a}^\dagger\hat{a}, \tag{6.87}$$

where

$$\omega_r' = \omega_r - \frac{g^2}{\Delta - E_C/\hbar}, \quad \omega_q' = \omega_q + \frac{g^2}{\Delta}, \quad \text{and} \quad \chi = \frac{g^2}{\Delta} - \frac{g^2}{\Delta - E_C/\hbar}. \tag{6.88}$$

From this Hamiltonian, we can determine the spectrum in the dispersive regime, which is

$$E_\pm = \hbar(\omega_r' \pm \chi)n \pm \hbar\frac{\omega_q'}{2}, \tag{6.89}$$

where $E_\pm$ is the energy for $|\pm, n\rangle$.

We can see that the first term of Eq. (6.89) looks like the spectrum of a harmonic oscillator but with a frequency that depends on the state of the qubit. This will be the basis of qubit readout in circuit QED, which we discuss in detail in Section 6.7. For now, let's comment on the structure of the state-dependent **dispersive frequency shift**, χ, here. The first term in χ, g^2/Δ, is the result obtained for a pure two-level system. The second term is a correction for the limited anharmonicity of the transmon. To leading order, the magnitude of the transmon's anharmonicity is E_C. We see that for $E_C \gg \Delta$, i.e. large anharmonicity, the correction term tends to zero, and we recover the result for the two-level system. In the other limit, with $\Delta \gg E_C$, we instead find that the correction cancels the leading term and $\chi \approx 0$. This recovers the result that, although coupling harmonic oscillators will produce frequency shifts, those shifts are not state-dependent.

Unlike the on-resonance case, the dressed states in the dispersive regime are not maximally mixed states. This can be seen by substituting the definition of θ_n into Eqs. (6.82) and (6.83). For $\Delta \gg g\sqrt{n}$, we can perform the series expansions to find $\cos\left(\arctan\left(\frac{g\sqrt{n}}{\Delta}\right)\right) \approx 1$ and $\sin\left(\arctan\left(\frac{g\sqrt{n}}{\Delta}\right)\right) \approx \frac{g\sqrt{n}}{\Delta}$. Thus, we find

$$|+, n\rangle \approx C_+\left(|e, n-1\rangle + \frac{g\sqrt{n}}{\Delta}|g, n\rangle\right), \tag{6.90}$$

$$|-, n\rangle \approx C_-\left(|g, n\rangle - \frac{g\sqrt{n}}{\Delta}|e, n-1\rangle\right), \tag{6.91}$$

where $C_\pm$ are normalization constants.

The most straightforward advantage of working in the dispersive regime is a large enhancement of the qubit lifetime compared to the resonant regime. Recall that the resonator will greatly enhance signals at its resonant frequency, ω_r. This also applies to environmental

noise, including quantum fluctuations. If our qubit is in resonance with this enhanced noise, it will have a much shorter lifetime. Working at a frequency away from this peak, in the wings of the resonator response, exposes the qubit to greatly suppressed noise, which will increase its lifetime. From an engineer's point of view, we would describe this simply by saying the resonator filters the environmental noise. Connecting to the terminology of cavity QED, the reduction of the qubit lifetime by the resonant cavity is known as the Purcell effect (which we discuss in Section 6.8). The enhancement of the lifetime in the dispersive regime is sometimes referred to as the **anti-Purcell effect**.

A more subtle advantage is that working in the dispersive regime reduces the backaction of the readout on the qubit, minimizing the disturbance to the qubit state. As the state of the qubit affects the resonance frequency of the cavity, so does the state of the cavity affect the transition frequency of the qubit. This can be seen by grouping the interaction (last) term of Eq. (6.87) with the qubit term, which together look like a shift in the qubit energy proportional to the photon number $\hat{a}^\dagger\hat{a}$. We typically readout the system by driving the resonator with a coherent state, which is a superposition of different photon numbers. This implies that the readout inherently drives fluctuations of the qubit frequency, which we want to minimize. Some amount of backaction is required in all quantum measurements, and the backaction implied by Eq. (6.87) can approach the quantum limit. However, if the coupling is too strong – for instance, because the detuning is too small – higher-order processes can contribute additional backaction without improving the measurement.

We end this section by enumerating different regimes of the Jaynes–Cummings model which are often referred to in the literature. If we let γ refer to the decoherence rate of the qubit, and κ the same for a cavity, then we can compare them to the respective frequencies ω_q, ω_r and the interaction strength g. In the **weak coupling regime**, where $g \ll \gamma, \kappa, \omega_q, \omega_r$, decoherence dominates the coherent dynamics between the qubit and the cavity represented by g. In the **strong coupling regime**, where $\gamma, \kappa \ll g \ll \omega_q, \omega_r$, the truly quantum dynamics of light–matter coupling can be observed. The strong coupling regime still generally represents a perturbative coupling between light and matter. In the regime $\gamma, \kappa \ll g \sim \omega_q, \omega_r$, sometimes called the **ultrastrong coupling** regime, the rotating-wave approximation breaks down and the coupling is no longer perturbative. This regime has only recently been observed experimentally.

6.5 Initialization

Superconducting qubits are initialized by brute-force cooling of the qubits to the ground state. A characteristic frequency of 5 GHz implies that the qubits must be cooled to a temperature $T \ll \hbar\omega/k_B \sim 250$ mK. This is far below the temperature of the liquid helium, ~4 K, used for the superconducting magnets in Chapter 3. We therefore require a specialized cryostat, a **dilution refrigerator** that can reach base temperatures of 10 mK. Other types of cryostats can reach the low temperatures required, but dilution refrigerators are preferred because they offer continuous operation, remaining at low temperatures for periods of several months.

Despite the ultra-low temperatures achieved by the dilution refrigerator, experimentalists typically find that the residual excitation of the excited state is much higher then would be predicted by simple thermodynamic calculations. There are a number of possible reasons for this, including stray electromagnetic radiation that reaches the qubits from higher temperatures. A recent strategy to mitigate this has been to use real-time feedback to improve the quality of the ground-state preparation. These are often called **active reset protocols**. The basic idea is to perform a high-fidelity measurement of the qubit's state, and if the qubit is found to be excited, to apply a π-pulse to flip the qubit to the ground state. This technique relies both on having (nearly) quantum-limited amplifiers[5] for the readout as well as high-speed digital electronics that can analyze the readout result and apply the conditional π-pulse in a time much less than the qubit's T_1.

6.6 Qubit Control

Having initialized our qubit, we turn to controlling it. First, we explain how single-qubit gates can be implemented using a microwave drive (Section 6.6.1). In Section 3.3.4 we introduced some techniques to mitigate pulse errors; we build on that discussion here. Next, we explain how two-qubit gates are implemented in Section 6.6.2. As we'll explain, the exact approach will depend on whether we're using tunable or fixed-frequency qubits.

6.6.1 Single-Qubit Gates

High-fidelity single-qubit gates have been implemented using a range of techniques. Broadly speaking, gates are implemented either by applying microwave control pulses or by fast tuning of the qubit transition frequencies. While we will focus on transmon qubits below, many of the techniques we describe are applicable to a range of different superconducting qubits.

Single-qubit gates, other than z-rotations (see below), are most commonly implemented by driving the qubits with resonant microwave signals that will drive Rabi oscillations. Apart from the control frequency, this is in strict analogy to single-qubit gates in NMR and ion traps.

All that needs to be done then is to show how we come to the Rabi Hamiltonian for a superconducting qubit. Let's start with the simplified example of the CPB. Consider the CPB Hamiltonian Eq. (6.57). We can couple the microwave drive through the same gate capacitor that we use for the gate voltage, which sets n_g. (In practice, we might use distinct gate capacitances to allow for better optimization.) For the signal applied to the gate capacitance, we then combine the DC bias and the microwave drive, giving $n_g = n_{g0} + \delta n_g \cos(\omega t + \phi)$. If we work around $n_{g0} = 1/2$ (and rotate to the qubit eigenbasis), Eq. (6.57) reduces to

$$\hat{H} = -\frac{E_J}{2}\hat{\sigma}_z + 4E_C\delta n_g \cos(\omega t + \phi)\hat{\sigma}_x, \tag{6.92}$$

[5] A quantum-limited amplifier adds the minimum amount of noise allowed by quantum mechanics during the amplification (measurement) process.

which is identical in form to the Rabi Hamiltonian (Eq. (3.10)) that we first considered in the context of NMR.

The same derivation for the transmon is somewhat more involved, but we can also derive the Rabi Hamiltonian for the transmon following a standard method in quantum optics. Consider the Hamiltonian of the transmon coupled to a resonator written in the two-level approximation but before the rotating-wave approximation, Eq. (6.77):

$$\hat{H}_{\mathrm{JC}} := \hbar\omega_r\hat{a}^\dagger\hat{a} - \frac{\hbar\omega_q}{2}\hat{\sigma}_z - \hbar g\hat{\sigma}_x(\hat{a}^\dagger - \hat{a}). \tag{6.93}$$

We now take the classical limit of the oscillator. We do so by essentially taking the partial expectation value of the field with a coherent state at the frequency ω with a large amplitude $|\alpha\rangle$. In the interaction frame of the oscillator, where $\hat{a}$ and $\hat{a}^\dagger$ pick up an explicit time-dependent phase, we find

$$\langle\alpha|\hat{H}_{\mathrm{JC}}|\alpha\rangle = -\frac{\hbar\omega_q}{2}\hat{\sigma}_z - 2\hbar g|\alpha|\sin(\omega t + \phi)\hat{\sigma}_x. \tag{6.94}$$

Up to a phase, we see that this is again just our familiar Rabi Hamiltonian. As an aside, we note that in going from the second-quantized equation to the semiclassical Rabi Hamiltonian, we are essentially ignoring the vacuum fluctuations of the field.

If we're using tunable transmons we can also implement z-axis rotations by directly tuning the value of ω_q so that $\omega_q - \omega_d \neq 0$. This can be done by inductively coupling another transmission line to the loop of the transmon's SQUID. A fast pulse on that line will create a fast-flux pulse which detunes the qubit. By controlling the amount of detuning and the length of the pulse, we can control the accumulated phase, i.e. the z-rotation angle. While it's possible to implement z-gates in this way, it's now common to use the book-keeping gates introduced in Section 3.3.3.

There are a variety of techniques used to address multiple qubits in a single processor. These generally combine a mix of frequency multiplexing, meaning that the qubits are designed to have different frequencies so a given pulse is only resonant with one qubit, and individual wiring, meaning that each qubit (or a small number of them) has its own microwave drive line. As processors get larger, bringing signals to internal qubits is challenging in a purely 2D architecture. Conventional (classical) processors have many layers of wiring with insulating layers in between, allowing for arbitrary routing and connections. It has generally been found that these insulators are lossy and add significant decoherence to quantum processors. Solving this problem is currently a very active field of research.

An important source of infidelity for transmons is leakage to the higher energy states that we have so far ignored. As with other implementations, we can use pulse shaping to reduce this leakage and improve the fidelity of our single-qubit gates. The anharmonicity of a transmon is small, 200–300 MHz compared to the qubit frequencies, which are on the order of gigahertz. Since the control pulses have a finite width in time, they also have a finite bandwidth in frequency, with the bandwidth inversely proportional to the width of the pulse in time. If the tail of the pulses' bandwidth overlaps with the transition frequency from $|1\rangle$ to $|2\rangle$, we can get excitations out of the computational basis. The simplest way to prevent this is just to use longer pulses and thus smaller bandwidth, but this creates a trade-off with the coherence time of the qubit. A next step is to consider pulse shaping.

For instance, rectangular pulses have a spectrum that decays very slowly ($1/f$) in frequency, while a pulse with a Gaussian shape in time also has a Gaussian spectrum, meaning the spectrum decays exponentially.

More sophisticated pulse-shaping techniques, based on optimal control theory, have become increasingly common. One very common example is the Derivative Removal via Adiabatic Gate (DRAG) technique. While the derivation of the DRAG protocol is beyond the scope of this book, this technique has allowed for single-qubit gates to be routinely implemented with greater than 0.99 fidelity.

6.6.2 Two-Qubit Gates

Numerous proposals exist for implementing two-qubit gates in superconducting systems, many of which have been demonstrated and have achieved high fidelities. At the time of writing this text, there is no dominant two-qubit gate design, and it's still an active area of research. Below we give an overview of the different types and focus on two well-developed and illustrative examples.

In many of the previous chapters, we implemented our two-qubit gates by regulating a natural interaction term in the system. Here, we need to first engineer the interaction or coupling term using different circuits. Transmon qubits are typically coupled with a capacitor. We previously derived the interaction Hamiltonian for capacitive coupling between the transmon and a resonator [$\hbar g(\hat{\sigma}_+\hat{a}+\hat{\sigma}_-\hat{a}^\dagger)$ from Eq. (6.77)] when we discussed the Jaynes–Cummings model in Section 6.4.3. The derivation for two transmons is nearly identical, so we just write the result,

$$\hat{H} = \hbar g_C(\hat{\sigma}_+^{(1)}\hat{\sigma}_-^{(2)} + \hat{\sigma}_-^{(1)}\hat{\sigma}_+^{(2)}), \tag{6.95}$$

where

$$\hbar g_C \coloneqq \frac{\sqrt{2}e^2 C_c}{C_1 C_2}\left(\frac{E_{J1}E_{J2}}{E_{C1}E_{C2}}\right)^{1/4}. \tag{6.96}$$

This expression describes the exchange of a single excitation between the two transmons. It is valid in the context of a rotating-wave approximation which assumes $|\Delta| = |\omega_{q1} - \omega_{q2}| \ll g_C$. Other couplings can be used when controlling other types of qubits, e.g. inductive couplings can be used with flux qubits. For the most common forms of coupling, the final interaction Hamiltonian remains in the same form, albeit with a different detailed expression of the coupling strength.

To go from an interaction to a gate, we need to be able to turn the interaction on and off in a controlled fashion. One possibility is to use a tunable coupling element, like a tunable capacitor or inductor, which would allow for the direct tuning of g_C. An alternative approach is to tune the qubit frequencies, adjusting the ratio of g_C to Δ (Fig. 6.18). When $g_C \gg |\Delta|$, the interaction is as described above, i.e. excitations are swapped between the qubits. In the other regime, $g_C \ll |\Delta|$, the rotating-wave approximation is no longer valid and the coherent swapping is strongly suppressed. In this way, we can effectively turn the interaction on and off, despite the constant presence of the fixed capacitive coupling.

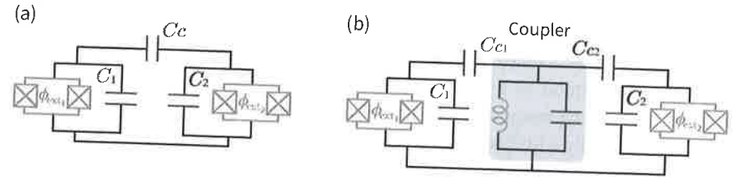

Fig. 6.18 **Transmon couplings.** (a) Direct capacitive coupling of tunable transmons. (b) Coupling of tunable transmons via a coupler.

Let's consider the type of gate produced by turning the capacitive coupling on for a specified time. Consider the action of this coupling written as a unitary in the computational basis

$$U_C(t) = \exp\left(-ig_C t(\hat{\sigma}_+^{(1)}\hat{\sigma}_-^{(2)} + \hat{\sigma}_-^{(1)}\hat{\sigma}_+^{(2)})\right) = \begin{bmatrix} 1 & 0 & 0 & 0 \\ 0 & \cos(g_C t) & -i\sin(g_C t) & 0 \\ 0 & -i\sin(g_C t) & \cos(g_C t) & 0 \\ 0 & 0 & 0 & 1 \end{bmatrix}. \tag{6.97}$$

If we choose our time $t = \pi/2g_C$, we get the so-called iSWAP gate,

$$U_C\left(\frac{\pi}{2g_C}\right) = \begin{bmatrix} 1 & 0 & 0 & 0 \\ 0 & 0 & -i & 0 \\ 0 & -i & 0 & 0 \\ 0 & 0 & 0 & 1 \end{bmatrix} =: \text{iSWAP}. \tag{6.98}$$

Its name follows from the fact that it swaps an excitation between the two qubits while adding an extra phase of i. From this, we can create the entangling $\sqrt{i\text{SWAP}}$ gate, which is created from the same interaction done for half the time, $U_C(\frac{\pi}{4g_C})$. Applied to the $|01\rangle$ state, the $\sqrt{i\text{SWAP}}$ gate prepares a Bell state.

Implementing two-qubit gates with tunable qubits has some notable challenges. The first is that the added tunability introduces another control parameter and, thus, introduces another channel for noise in the system, potentially decreasing the transmon's coherence time. Second, the performance of the gates relies very sensitively on the shape of the fast-flux pulses used for tuning, which often have nanosecond timescales. It's very difficult to control or even measure the exact shape of the pulses that reach the qubits, since they travel through long cables with frequency-dependent loss along with a number of other microwave components. Designing gate protocols that mitigate these problems is an active area of research.

Part of the issue with the pulse shapes of the fast-flux pulses used for tunable-qubit gates is that they are extremely broadband, with frequency components ranging from 0 Hz to several gigahertz. An alternative approach is to use more narrowband microwave pulses to create two-qubit gates, similar to how single-qubit gates are done with microwave pulses. A clear disadvantage of using more narrowband pulses is that they will tend to produce slower gates, but this is a natural trade-off between the speed and precision of control pulses.

There are a variety of approaches to microwave-based two-qubit gates, with prominent examples being **parametric gates** and **cross-resonance gates**. Parametric gates use a tunable qubit or a tunable coupler, but now tune them at microwave frequencies, often at the frequency difference between a pair of qubits. Cross-resonance gates instead work entirely with fixed frequency qubits, avoiding the extra decoherence channel associated with tunability. We will consider cross-resonance gates in more detail now.

The cross-resonance gate still requires that the qubits have a fixed coupling to each other, e.g. capacitive coupling for transmons. Unlike with tunable-qubit gates, however, the qubits are strongly detuned from each other, i.e. $|\Delta| \gg g_C$. The gate is implemented by driving one qubit, the control qubit, at the frequency of the other qubit, the target qubit. Essentially, the control qubit acts as a state-dependent filter of the Rabi drive, changing the drive amplitude and phase seen by the target qubit. Roughly the control qubit acts as a filter with a center frequency equal to its transition frequency, which is ω_{q1} in its ground state and $\omega_{q1} - \alpha$ in its excited state. As we will see in detail below, the state-dependent driving of the target qubit can entangle it with the control qubit.

We begin again with the Hamiltonian of two qubits coupled via a capacitor and add a drive on the first qubit,

$$\hat{H} = -\frac{\hbar\omega_{q1}}{2}\hat{\sigma}_z^{(1)} - \frac{\hbar\omega_{q2}}{2}\hat{\sigma}_z^{(2)} + \hbar g_C(\hat{\sigma}_+^{(1)}\hat{\sigma}_-^{(2)} + \hat{\sigma}_-^{(1)}\hat{\sigma}_+^{(2)}) + \hbar\Omega_R(t)\cos(\omega_{d1}t)\hat{\sigma}_x^{(1)}, \tag{6.99}$$

where ω_{d1} is the frequency of the drive on the first qubit. To better see the effect of the driving term, we use a transformation like the one introduced in Eq. (6.86) and explored in the exercises. Doing so, we find the driving term becomes

$$\hbar\Omega_R(t)\cos(\omega_{d1}t)\left(\hat{\sigma}_x^{(1)} + \frac{g_C}{\Delta}\hat{\sigma}_z^{(1)}\hat{\sigma}_x^{(2)}\right). \tag{6.100}$$

We then see that the effective amplitude and phase of the Rabi drive on qubit 2, that is, the coefficient of the $\hat{\sigma}_x^{(2)}$, depends on the state of qubit 1.

The cross-resonance gate can then be represented by the unitary matrix

$$U_{\mathrm{CR}}(\theta) = \exp\left(-i\frac{\theta}{2}\hat{\sigma}_z^{(1)}\hat{\sigma}_x^{(2)}\right) = \begin{bmatrix} \cos\theta/2 & -i\sin\theta/2 & 0 & 0 \\ -i\sin\theta/2 & \cos\theta/2 & 0 & 0 \\ 0 & 0 & \cos\theta/2 & i\sin\theta/2 \\ 0 & 0 & i\sin\theta/2 & \cos\theta/2 \end{bmatrix}, \tag{6.101}$$

where θ depends on the strength of the coupling. This is clearly a two-qubit entangling gate.

6.7 Measurement

By far the most common form of superconducting qubit readout derives from circuit QED. This **dispersive readout** involves inferring the state of the qubit from its effect on a readout cavity to which it is coupled. First demonstrated for charge qubits and transmons, it has been adapted to a wide variety of qubits, including semiconductor qubits.

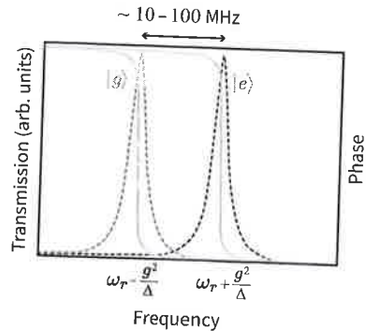

Fig. 6.19 **Dispersive readout.** The resonator's frequency experiences a shift depending on the qubit's state. The frequency of the resonator will be either $\omega_r' + \chi$ or $\omega_r' - \chi$, depending on if the qubit is in the $|e\rangle$ or $|g\rangle$ state, respectively. This property allows us to measure the qubit's state by probing the resonator with a microwave tone to infer its resonance frequency. The figure shows the magnitude (left axis) and phase response (right axis) of the resonator for the two-qubit states. If we probe at either one of the shifted cavity frequencies, the state information will be encoded in the magnitude of the microwave signal. If we probe at the bare cavity frequency, with $\omega_d = \omega_r'$, the information will instead be in the phase of the microwaves.

To understand how dispersive readout is done, we'll return to the Hamiltonian of our transmon in the dispersive regime, Eq. (6.87). By collecting certain terms we can write this as

$$\hat{H}_{\mathrm{disp}} = \hbar(\omega_r' - \chi\hat{\sigma}_z)\hat{a}^\dagger\hat{a} - \frac{\hbar\omega_q'}{2}\hat{\sigma}_z. \tag{6.102}$$

Written in this way, it's clear that the resonator's frequency experiences a shift depending on the qubit's state. The frequency of the resonator will be either $\omega_r - \chi$ or $\omega_r + \chi$, depending on if the qubit is in the $|e\rangle$ or $|g\rangle$ state, respectively (Fig. 6.19). This property also allows us to measure the qubit's state by measuring the frequency of the resonator.

One could imagine measuring the resonance frequency by measuring at many different frequencies and fitting a resonance curve, but this is inefficient and unnecessary. It is sufficient to probe the resonator at a single, well-chosen frequency. Perhaps the most obvious strategy is to send a microwave pulse to the resonator at one of its possible frequencies, $\omega_r \pm \chi$, and measure the resulting transmission intensity. For example, we could probe the resonator with a pulse of frequency $\omega_d = \omega_r - \chi$. If the transmission of the microwaves through the cavity is large, then we know that the frequency of the pulse matched that of the resonator, and so the qubit is in the $|g\rangle$ state. On the other hand, if the transmission of the microwaves is near zero, then we know that the qubit is in the $|e\rangle$ state. Alternatively, we could probe the resonator with a frequency of $\omega_d = \omega_r$. In this case, the transmitted magnitude will be the same for both qubit states. However, the microwave pulse will experience a phase shift as it moves through the resonator, and this phase shift will now depend on the qubit states (This phase shift will depend on the frequency of the resonator, and thus on the qubit's state – see Fig. 6.19.) If the dispersive shift of the resonator is large compared to its linewidth, the microwaves will experience a $\pi/2$ or $-\pi/2$ phase shift when

the qubit is in the $|e\rangle$ or $|g\rangle$ state, respectively. (Note that in this limit, most of the probe signal is reflected since it is off-resonance with the shifted cavity frequency, implying that it's better to measure the reflected signal instead.) The change in phase can be measured by comparing the output pulse to a phase reference, e.g., using a mixer. While both approaches are possible, the magnitude-based approach has some disadvantages. Most significantly, it strongly entangles the state of the qubit with the state of the readout cavity, since the two states of the cavity corresponding to the two qubit states are very different. This can be undesirable.

We have reduced the problem of discriminating the qubit states to that of measuring the phase of the microwave signal. How well we can do that depends on how large our microwave signal is compared to how noisy our measurement apparatus is. That is, it depends on the signal-to-noise ratio of a microwave phase measurement. Detailed calculations and experiments show that the power of the probe signal must be kept very low, in the tens of photons level, otherwise the measurement backaction is too large and the qubit state is destroyed before being measured. At this power, even the best semiconductor microwave amplifiers are too noisy. This fact has driven the development of a new generation of superconducting amplifiers, known broadly as **Josephson parametric amplifiers**. These amplifiers now routinely operate near the standard quantum limit of noise, which implies only adding a unit of vacuum noise (half of a photon) during the measurement process.

6.8 Noise

We conclude our final chapter on a quantum hardware with a deeper dive into noise and decoherence. In Section 3.7 we introduced the effects of noise and decoherence using the phenomenological T_1 and T_2 decay times added to the Bloch equations. In Section 6.8.1 we explore the microscopic physical processes that underlie T_1 and T_2. Using superconducting qubits as an example, we will derive explicit formulas for T_1 and T_2. Further, we discuss prominent environmental noise sources in solid-state devices in Section 6.8.2. We emphasize that the general discussion and techniques in this section apply to other types of qubits. This discussion of noise is a natural bridge to our final chapter on quantum benchmarking, which discusses the ways in which we understand how well our qubits are performing.

6.8.1 Decoherence

The conceptual starting point for exploring decoherence is that we imagine a small quantum system, e.g. our qubit, coupled to a very large quantum system, i.e. the environment (often called the "bath" or "reservoir" in this context). The total quantum system may evolve coherently, but since we cannot keep track of a very large number ($\sim 10^{23}$) of degrees of freedom in the environment, we are left to consider only its average properties. As we explained in Section 2.3.1, we express this by saying that we trace over the degrees of freedom of the environment. When we do this, the state of the qubit must be represented by a mixed-state density operator.

This conceptual description can be translated into mathematical form in a very general way. In order to find convenient analytical results, we must make two important approximations. First, in the **weak-coupling approximation**, we assume that the coupling between the qubit and environment is weak, which implies that we can treat the coupling to the environment perturbatively. Second, we assume that the environment is so large that its state is essentially unaffected by its interaction with the qubit. In this way, the state of the environment has no memory of anything that the qubit has done in the past, that is, the environment is memoryless. This is known as the **Markovian approximation**. When the Markovian approximation is valid, the environment and its dynamics are said to be **Markovian**.

With these approximations (and some others), the equations of motion for the (reduced) density matrix of the qubit can be derived, leading to a so-called **master equation**. The full quantum version of the Bloch equations, including T_1 and T_2, are an example of a master equation. We will take a simplified, physical approach to deriving T_1 and T_2, giving results that agree with the full master equation calculations given the stated approximations.

We take the Hamiltonian of our qubit, $\hat{H}(\lambda)$, to depend on a number of parameters (operators), λ ($\hat{\lambda}$), such as the gate charge, n_g, of the CPB. The environment then introduces noise (fluctuations) in these parameters, which in turn causes $\hat{H}(\lambda)$ to fluctuate. This is the physical source of decoherence. Since we assume the coupling between the qubit and environment is weak, we take the coupling Hamiltonian between the qubit and the environment to have the form

$$\hat{H}_c = \frac{\partial \hat{H}}{\partial \lambda} \Delta\hat{\lambda}, \tag{6.103}$$

where $\Delta\hat{\lambda}$ is an operator representing the environmental degrees of freedom.

To understand the effect of this coupling, it is useful to now restrict the qubit Hamiltonian to the two-level approximation. With this restriction, we define

$$\frac{\partial \hat{H}}{\partial \lambda} = -\frac{1}{2}\vec{\sigma} \cdot \vec{D}, \tag{6.104}$$

where the components of $\vec{D}$ can be found as $D_i = -\mathrm{tr}\left(\hat{\sigma}_i \frac{\partial \hat{H}}{\partial \lambda}\right)$ in the computational basis of the qubit. Written in this form, it is clear that D_z leads to fluctuations in the qubit energy, i.e. dephasing parameterized by T_2. Conversely, the transverse components, D_x and D_y, are responsible for qubit transitions, i.e. relaxation and excitation (at finite temperature) parameterized by T_1.

We can now directly write down the relaxation rate, $\Gamma_R = 1/T_R$, and excitation rate, $\Gamma_E = 1/T_E$, using Fermi's golden rule (see Section 5.2.2), which describes the transition between discrete levels of a system (the qubit) coupled to a continuum (the environment). Fermi's golden rule says that the transition rate is proportional to the magnitude squared of the matrix element connecting the two discrete levels multiplied by the density of states of the continuum at the transition energy. We find

$$\Gamma_{R/E} = \frac{\pi}{2\hbar^2} D_\perp^2 S_\lambda(\pm\omega_q), \tag{6.105}$$

where $D_\perp = \sqrt{|D_x|^2 + |D_y|^2} = 2|\langle 0|\frac{\partial \hat{H}}{\partial \lambda}|1\rangle|$ is the transverse component of $\vec{D}$ and $S_\lambda(\omega)$ is the **spectral density of fluctuations** of λ, defined as

$$S_\lambda(\omega) = \frac{1}{2\pi}\int_{-\infty}^{\infty} d\tau \langle \Delta\hat{\lambda}(0)\Delta\hat{\lambda}(\tau)\rangle \exp(-i\omega\tau). \tag{6.106}$$

(Note that other normalizations are possible.) The spectral density measures the strength of fluctuations in λ as a function of frequency but, through the fluctuation–dissipation theorem, also quantifies the density of states in the environment which can absorb energy from the qubit.

Classically, $S(\omega)$ is a symmetric function of frequency, but this is not the case in the quantum description. In fact, for the environment in thermal equilibrium, we have $S(-\omega)/S(\omega) = \exp(-\hbar\omega/kT)$. We can interpret the negative frequency side of the spectrum as representing real excitations in the environment, which only have nonzero magnitude at finite temperature. Conversely, the positive frequency side includes vacuum fluctuations, which can induce spontaneous emission (relaxation) even at zero temperature, and represents the ability of the environment to absorb energy from the qubit. At finite temperature, it is the quantity $\Gamma_1 = 1/T_1 = \Gamma_R + \Gamma_E$ that enters into the Bloch equations. At zero temperature, $\Gamma_1 = \Gamma_R$ and is often referred to as the relaxation rate, even though it generally parameterizes the effects of both relaxation and excitation.

The treatment of dephasing depends on the origin of the fluctuations. That is, we can imagine λ as a purely classical control parameter, like a gate or flux bias, with purely classical fluctuations. Alternatively, we can treat the fluctuations as arising from quantum fluctuations in the environment. We outline both treatments here.

In the classical case, $\hat{\Delta\lambda} = \Delta\lambda$ and its coupling through D_z just produces fluctuations in the qubit energy level. A superposition of the qubit states then acquires a phase

$$\varphi(t) = \int_0^t \omega_q dt' = \langle\omega_q\rangle t + \delta\varphi(t) \tag{6.107}$$

with

$$\delta\varphi(t) = \frac{D_z}{\hbar}\int_0^t \Delta\lambda(t')dt'. \tag{6.108}$$

We see then that the fluctuations in the qubit's energy lead to a random walk in the qubit phase. We can compute the average of this phase for an ensemble of measurements, finding

$$\langle\exp(i\delta\varphi(t))\rangle = \exp\left(-\frac{1}{2}\langle\delta\varphi(t)^2\rangle\right), \tag{6.109}$$

where we have assumed that the fluctuations of $\Delta\lambda$ have a Gaussian distribution. Importantly, averaging over the ensemble of noise converts the oscillatory function on the left to a decaying exponential function on the right.

We are left, then, to calculate the variance of the phase fluctuations $\langle\delta\varphi(t)^2\rangle$. We can write the general result

$$\langle\delta\varphi(t)^2\rangle = \left(\frac{tD_z}{\hbar}\right)^2\int_{-\infty}^{\infty} d\omega S_\lambda(\omega)\,\mathrm{sinc}^2(\omega t/2), \tag{6.110}$$

where $\mathrm{sinc}(x) = \sin(x)/x$. The sinc function arises from the filtering effect of integrating $\Delta\lambda$, and indicates that fluctuations of $\Delta\lambda$ within a bandwidth of $\sim 1/t$ contribute to dephasing.

To evaluate the integral, we need to specify the form of $S_\lambda(\omega)$. We can show that the Markovian approximation mentioned above for the environment implies that $S_\lambda(\omega)$ is approximately constant at relevant frequencies. (That is, the spectrum of the noise is "white" which implies that its correlation function is a delta function.) With this approximation, we find

$$\exp\left(-\frac{1}{2}\langle\delta\varphi(t)^2\rangle\right) = \exp(-\Gamma_\varphi t) \tag{6.111}$$

with the dephasing rate

$$\Gamma_\varphi = \pi\left(\frac{D_z}{\hbar}\right)^2 S_\lambda(\omega = 0). \tag{6.112}$$

We have finally recovered a simple exponential decay of the qubit coherence, consistent with the form of the Bloch equations. We note that this "pure" dephasing is added to the homogeneous contribution, $\Gamma_1/2$, to give the total rate $\Gamma_2^* = \Gamma_1/2 + \Gamma_\varphi$, which would be observed, e.g. in a Ramsey experiment.

In fact, as we discuss in more detail below, solid-state systems often have noise that is not white. Instead, so-called $1/f$ noise (read "one over f") is common, which has a spectrum $S_\lambda(\omega) \sim 1/\omega$. We've seen above that dephasing is dominated by the low-frequency components of the noise spectrum, making $1/f$ noise particularly problematic for dephasing. The strong frequency dependence of $1/f$ noise breaks the assumptions of the Markovian approximation, and we can no longer recover a simple exponential decay. That is, we cannot define a simple dephasing rate, Γ_φ. Still, we can calculate the decay and find instead a Gaussian envelope:

$$\exp\left(-\frac{1}{2}\langle\delta\varphi(t)^2\rangle\right) = \exp\left(-\frac{1}{2}\left(\frac{D_z}{\hbar}\right)^2 t^2\langle\Delta\lambda^2\rangle\right), \tag{6.113}$$

where $\langle\Delta\lambda^2\rangle$ is the variance of $\Delta\lambda$.

We will now briefly discuss the quantum treatment of dephasing. To do this, we need to have a more detailed model of the environment. One standard approach is to treat the environment as a bath of harmonic oscillators with a dense (approximately continuous) distribution of frequencies. This approach is often called the **spin-boson model**, with a two-level system (a spin or qubit) interacting with the bath of bosonic excitations of the oscillators. Describing the bath degrees of freedom as harmonic oscillators may seem contrived but, in fact, it is rather general. Even for a complicated nonlinear system, the dynamics of small deviations or fluctuations from the steady state can generically be described by a harmonic oscillator. Within the limits of the approximations for the master equation, e.g. weak coupling, modelling the bath as harmonic oscillators is a well-justified approximation.

With this description of the environmental bath, we can now write down a simple linear form for the noise operator:

$$\Delta\hat{\lambda} = \sum_n (\lambda_n^* \hat{b}_n^\dagger + \lambda_n \hat{b}_n), \tag{6.114}$$

which is appropriate in the weak coupling limit. Here, $\hat{b}_n$ is the annihilation operator for the nth environmental oscillator and λ_n is its coupling coefficient.

Conceptually, the quantum calculation of dephasing proceeds in a very similar manner as the classical calculation, although the mathematical details are beyond the scope of this book. In the end, though, we arrive at the same form as in Eqns. (6.111) and (6.112), the difference being that $S_\lambda(\omega)$ is now interpreted as a quantum spectral density, which includes quantum noise. The most important difference, then, is that the quantum treatment predicts a finite dephasing rate even at zero temperature, where the classical noise would go to zero.

Everything stated so far applies equally well to any qubit. As a concrete example, lets consider how classical noise in n_g, the scaled gate voltage, effects the CPB or transmon, both of which are described by the Hamiltonian in Eq. (6.50). This noise could come from, e.g. noise in the room-temperature electronics used to control the gate voltage. We can also use noise in n_g to model (classical) charge noise in the qubit's environment, which will couple in the same way.

The first step is to calculate the components of $\vec{D}$. We find first of all that $\partial\hat{H}/\partial n_g = -8E_C(\hat{n} - n_g)$. Projecting onto the qubit subspace $\{|e\rangle, |g\rangle\}$, we find

$$D_\perp = 16E_C|\langle g|\hat{n}|e\rangle| \quad ; \quad D_z = -8E_C\left(\langle e|\hat{n}|e\rangle - \langle g|\hat{n}|g\rangle\right). \tag{6.115}$$

In the CPB regime ($E_C \gg E_J$), it is instructive to further simplify by explicitly calculating the matrix elements in these expressions. To do so, we first write the qubit eigenstates in the charge basis $\{|1\rangle, |0\rangle\}$ as

$$|g\rangle = \cos(\theta/2)|0\rangle + \sin(\theta/2)|1\rangle, \tag{6.116}$$

$$|e\rangle = \sin(\theta/2)|0\rangle - \cos(\theta/2)|1\rangle, \tag{6.117}$$

with the mixing angle

$$\theta = \cos^{-1}\left[\frac{4E_C(1-2n_g)}{\hbar\omega_q}\right]. \tag{6.118}$$

We then find $D_\perp = 8E_C|\sin\theta|$ and $D_z = -8E_C\cos\theta$, which gives the rates

$$\Gamma_{R/E} = \frac{32\pi}{\hbar^2}E_C^2\sin^2\theta S_{n_g}(\pm\omega_q) = \frac{2\pi}{\hbar^2}e^2\kappa_g^2\sin^2\theta S_V(\pm\omega_q), \tag{6.119}$$

$$\Gamma_\varphi = \frac{64\pi}{\hbar^2}E_C^2\cos^2\theta S_{n_g}(\omega_q = 0) = \frac{4\pi}{\hbar^2}e^2\kappa_g^2\cos^2\theta S_V(\omega_q = 0), \tag{6.120}$$

where on the far right e is the electron's charge, $\kappa_g = C_g/C_\Sigma$ is the coupling of the CPB to the fluctuations, and $S_V(\omega)$ is the spectral density of the (unscaled) voltage fluctuations.

We can make a couple of comments on the form of these rates. First, if we take the magnitude of $S(\omega)$ as a given, we can still control the decoherence rates by reducing the coupling of the qubit to the environment by reducing κ_g. If we only had one gate, this would also, for instance, reduce the Rabi frequency of the qubit for a given drive strength, that is, it would increase the single-qubit gate time of the qubit. This creates an engineering trade-off, balancing gate speed versus decoherence rate. However, we usually have the ability to increase the output power of the room-temperature microwave generator that drives the qubit in such a way as to keep the Rabi frequency unchanged.

Further, consider the two bias points $n_g = 0$ and $n_g = 1/2$, which gives $\theta \approx 0$ and $\theta = \pi/2$, respectively. At $n_g = 0$, we see that $\Gamma_{R/E} \approx 0$ while Γ_φ is maximized. This makes sense, because here the qubit states are very close to pure charge states, such that fluctuations of the gate charge predominately change the qubit energy, causing dephasing. Conversely, at $n_g = 1/2$ we find that $\Gamma_\varphi = 0$ while $\Gamma_{R/E}$ is maximized. We can understand that $\Gamma_\varphi = 0$ at this point in two ways. First, referring to Fig. 6.10, we see that $\partial\omega_q/\partial n_g = 0$ at this point, so the qubit energy is insensitive (to first order) to charge fluctuations at this bias point. Second, we can observe that the matrix elements that go into D_z in Eq. (6.115) are just the expectation values of the normalized charge of the qubit states, implying that D_z for charge noise is just proportional to the difference of the charge of the qubit states. At $n_g = 1/2$, the charge of the qubit states is equal, so the charge noise doesn't couple to the qubit energy. This is an example of what is generally called a **decoherence-free subspace**. Because of the presence of a variety of prominent noise sources in the solid-state environment, as described below, finding and exploiting this type of insensitive point, or "sweet spot," has been critical to the advancement of superconducting qubits.

6.8.2 Physical Noise Sources

In this section we review a number of different physical noise sources that affect solid-state qubits. This includes superconducting qubits, but also applies to other types, e.g. semiconductor quantum dots.

Dissipative elements in our quantum circuit, e.g. bias resistors, will add noise to the system. This is a fundamental result known as the **fluctuation–dissipation theorem**. In circuits, we typically describe dissipation in terms of resistors, and this noise is referred to as Johnson–Nyquist noise. Classically, or for frequencies $\omega \ll kT/\hbar$, the spectral density of this noise is white and proportional to temperature. The quantum version for $\omega \gg kT/\hbar$ is vacuum noise, with a spectral density proportional to frequency for positive frequencies and approximately zero for negative frequencies. For a resistance, R, which can also be the real part of an impedance $\mathrm{Re}\,Z(\omega)$, the full quantum spectral density of the voltage fluctuations of the resistor is

$$S_V(\omega) = \frac{\hbar|\omega|}{2\pi}\left[\coth\left(\frac{\hbar\omega}{2kT}\right) + 1\right]R. \tag{6.121}$$

We note that even though the noise is not white in the quantum regime, its variation is typically small enough in the bandwidth of the coupling to the qubit that the Markovian results apply. That is, we can define simple exponential decoherence rates for Johnson–Nyquist noise.

In circuit QED, the microwave transmission line used to couple to the qubit is taken to have a real 50 Ω impedance and therefore generates Johnson–Nyquist noise. In fact, we typically operate circuit QED systems in the dispersive regime so that the readout cavity filters the Johnson–Nyquist noise of the transmission line. If the cavity were instead on-resonance with the qubit, it would enhance the environmental noise, decreasing the qubit lifetime. This is known as the Purcell effect. Circuit QED systems often now incorporate

additional cavities in series with the readout cavity to further filter the Johnson–Nyquist noise. These are often referred to as Purcell filters.

A ubiquitous form of noise in solid-state systems is charge noise, which results in fluctuations in the $\hat{n}$ operator of our Hamiltonian. While the microscopic origin of charge noise isn't fully understood, it is generally thought to arise from mobile charges on the surface of the device or substrate – for instance, from charged defects moving between two defect states. Charge noise has an approximately $1/f$ spectrum. It can be shown that a $1/f$ spectrum arises naturally from an ensemble of two-state fluctuators distributed randomly in frequency. Each fluctuator contributes a Lorentzian spectrum centered at $f = 0$, with a bandwidth corresponding to the inverse switching time of the fluctuator, $1/\tau$. Incoherently adding these individual spectra produces an ensemble $1/f$ spectrum. In fact, in detailed measurements of charge noise, one can often find one or two charge fluctuators that are strongly coupled to the qubit, such that their Lorentzian spectra standout from the $1/f$ background.

Charge noise has been studied for decades in many types of systems, including superconducting and semiconducting systems, with a wide variety of materials. The magnitude has been found to be almost mystically universal, which can be expressed as

$$S_Q(\omega) = A_Q^2 \left(\frac{2\pi \times 1 \text{ Hz}}{\omega} \right)^{\gamma_Q}, \tag{6.122}$$

where $A_Q^2 \approx (10^{-3}e)^2/\text{Hz}$ and $\gamma_Q \approx 1$. The intransigence of charge noise was the motivation for the development of the transmon, which is relatively insensitive to charge noise compared to the CPB.

Another ubiquitous form of noise is flux noise, and it results in fluctuations in the $\hat{\phi}$ operator of our Hamiltonian. It is most problematic for flux qubits, but also affects tunable transmons. Like charge noise, flux noise has an approximately $1/f$ spectrum. Also like charge noise, its microscopic origin is not well understood, although it is generally thought to arise from magnetic defects, such as defect molecules with a net spin, that randomly change their orientation. The ensemble of two-state magnetic fluctuators leads to the ensemble $1/f$ flux noise, similar to the story for charge noise. As a last similarity, it is also mystically universal, with a spectral density given by

$$S_\Phi(\omega) = A_\Phi^2 \left(\frac{2\pi \times 1 \text{ Hz}}{\omega} \right)^{\gamma_\Phi}, \tag{6.123}$$

where $A_\Phi^2 \approx (1\mu\Phi_0)^2/\text{Hz}$ and $\gamma_\Phi \approx 0.8$–1.0.

While most of the electrons in the superconductor form into Cooper pairs, some electrons remain unpaired. These excitations from the ideal superconducting ground state are known as quasiparticles. (In fact, they are coherent superpositions of electrons and holes.) At finite temperatures, the number of quasiparticles in thermal equilibrium is determined by basic thermodynamics. At dilution refrigerator temperatures in aluminum, this thermal density should be vanishingly small. Experimentally, the density of quasiparticles is universally observed to be orders of magnitude higher than the thermal number. Stray black-body radiation leaking from higher temperature stages of the cryostat is one contribution to this nonequilibrium background. However, even in the most carefully shielded systems

a background remains. One potential culprit is ionizing radiation, either from natural, terrestrial radioactivity or from cosmic rays.

Quasiparticles can cause loss in a variety of ways. In superconducting films they can absorb and dissipate energy from the microwave fields of resonators and qubits. They can also tunnel through the Josephson junctions that make up the qubits, exchanging energy with the qubit and causing relaxation or excitation.

Circuit QED introduces another source of error: fluctuations in the resonator's residual photon number. Ideally, when not measuring the qubit, its readout resonator would have exactly $n = 0$. However, there can often be a small residual photon population due to either stray thermal photons or residual readout photons. While the photon number may have a well-defined average number, it will generally also fluctuate. In the dispersive regime, these photons affect the qubit through the Hamiltonian,

$$\hat{H}_{\text{disp}} = \hbar\omega_r'\hat{a}^\dagger\hat{a} - \frac{\hbar\omega_q'}{2}\hat{\sigma}_z - \hbar\chi\hat{\sigma}_z\hat{a}^\dagger\hat{a}. \tag{6.124}$$

The last term can be interpreted as a shift of the qubit frequency proportional to the number of photons in the resonator. Therefore, fluctuations of the photon number produce fluctuations of the qubit frequency, leading to dephasing. In detail, the spectral density is Lorentzian with a bandwidth of the cavity linewidth, κ. Since, typically, $\kappa \ll \omega_q$, these fluctuations don't contribute to relaxation. Conversely, since κ is generally much larger than the inverse measurement time, this noise looks effectively white in our dephasing integrals above, meaning that its noise can be described by a simple exponential dephasing rate.

Mitigating photon fluctuations is typically done with better cryogenic engineering. The goal here is to reduce the thermal photon fluctuations that come from the warmer parts of the fridge. This type of refinement includes adding material to absorb stray thermal photons, adding dissipative filters to assist with thermalization, and optimizing parameters of the cryogenic attenuators.

6.9 Conclusion

We conclude this chapter with a summary of how we can use superconducting circuits for quantum computing (Section 6.9.1) and a discussion on the strengths and weaknesses of computing with superconducting circuits (Section 6.9.2). For further reading on superconducting quantum computing, see Blais et al. (2021) or Krantz et al. (2019), and on superconducting physics, see Tinkham (2004) or Van Duzer and Turner (1981).

6.9.1 Summary

In superconducting qubit quantum computing, the qubits are encoded in the eigenstates of superconducting circuits whose energy spectrum is discrete, well separated, and anharmonic. A Josephson junction typically provides this anharmonicity. Many qubit architectures have been studied, and the transmon has been one of the most successful ones to date for quantum

Table 6.1 An overview of how a system of superconducting qubits can satisfy each of the DiVincenzo criteria for quantum computation

Criteria	Realization
1. A scalable physical system with well-characterized qubits	Qubit: electronic states of a superconducting circuit
2. The ability to initialize the state of the qubits to a simple fiducial state	Cooling in a dilution refrigerator
3. A universal set of quantum gates	One-qubit gates: resonant microwaves drive Rabi rotations Two-qubit gate: a combination of fast tuning pulses and microwave drives, or only microwaves
4. A qubit-specific measurement capability	Dispersive readout through a coupled resonator
5. Long relevant decoherence times, much longer than the gate operation time	Decoherence time: ~1 ms One-qubit gate time: 10–30 ns Two-qubit gate time: 10–100 ns

computing. We couple the transmon to a microwave waveguide resonator when controlling and measuring it. The study of this interaction is known as circuit QED, and the interaction is given by the Jaynes–Cummings Hamiltonian. To initialize the transmon, we cool it using a dilution refrigerator. Single-qubit control is achieved by applying microwave pulses to the qubit. There exist numerous proposals for two-qubit gates. Gates can be implemented, for example, by adjusting the frequency of tunable qubits or by driving the qubits with microwaves. Finally, sources of decoherence for superconducting qubits include Johnson–Nyquist noise, charge noise, flux noise, quasiparticles, and fluctuations in the resonator's residual photon number.

An overview of the contents of this chapter is provided in Table 6.1.

6.9.2 Relative Strengths and Weaknesses

There are certain key advantages to using superconducting qubits. A notable one is that, because the qubits are fabricated, we achieve a degree of tunability to the their properties, such as their energy levels and coupling strength. This feature also makes superconducting qubits more apt for quantum simulations. This tunability is not present when we are left to choose from the qubits nature gives us. On a related note, superconducting qubits can be made to have much larger dipole moments than natural atoms and thus more strongly couple to one another and to external controls. This has allowed for gates to be implemented faster than with trapped ions, while maintaining similar degrees of fidelity. These gates are also controlled with microwave technologies, which are well developed and commercially

available. High fidelity has also been achieved when performing qubit measurements. A final major appeal of superconducting qubits is that they are fabricated using techniques already used for silicon-based computer chips. The hope then is that the structure is already present to scale these quantum computers like we have classical computers.

Superconducting qubits also have disadvantages. First, they require being cooled to near absolute zero temperatures. The dilution refrigerators necessary to do this are costly and use an exotic gas, ^{3}He, which doesn't occur in large quantities in nature and has to be produced through an expensive process. The second challenge of superconducting qubits is that they generally have shorter coherence times than trapped ions. However, this drawback can be compensated for by their much faster gate times. In the early days of superconducting qubits, the decoherence times were very short (~ns); they're now on the order of milliseconds and still improving. The qubits' added tunability also brings its own challenge. Since the qubits are manufactured, there are variations in their properties and questions about reproducibility. This is unlike trapped ions, in which all the ions used are inherently identical. An issue with the popular transmon qubit is its limited anharmonicity, which requires care when performing qubit control and gates to avoid leakage.

6.10 Exercises

6.1 **Energy Scales:** Here we will consider some typical experimental energy scales of superconducting qubits.

(a) A typical tunnel junction has a capacitance per unit area of 50 fF/μm^2. Give the dimensions of a square tunnel junction with a Cooper-pair charging energy of $E_C/k_B = 30$ K.

(b) A typical current density for an aluminum Josephson junction is $J_c = 100$ A/cm^2. Give the dimensions of a Josephson junction with a Josephson energy of $E_J/h = 5$ GHz.

(c) Consider a CPB with $E_J/h = 5$ GHz biased at its degeneracy point $n_g = 1/2$. If the CPB is at $T = 250$ mK, what is the population of the first excited state when the system is in equilibrium? What temperature is needed for the population of the ground state to be greater than 99%?

6.2 **The Josephson inductance:** The constitutive relations of a Josephson junction are the Josephson relations

$$I = I_c \sin(\delta), \tag{6.125}$$

$$\frac{\mathrm{d}\delta}{\mathrm{d}t} = \frac{2e}{\hbar} V. \tag{6.126}$$

By comparing these to the constitutive relation for an inductor, show that the Josephson junction acts like an inductor for small oscillations. What is the expression for the inductance, the so-called Josephson inductance? With $J_c = 100$ A/cm^2, what is the Josephson inductance of a Josephson junction that is 200 nm by 200 nm? Is this a big or small inductance?